

Isolated Binary Black Hole Formation and Merger Rates from Galaxy Evolution

TYLER B. SMITH¹ AND MANOJ KAPLINGHAT¹

¹*Department of Physics and Astronomy
University of California, Irvine, CA 92697, USA*

ABSTRACT

The LIGO-Virgo-KAGRA (LVK) collaboration has detected 90 gravitational wave events and will detect many more in its fourth observing run. Binary black hole (BBH) systems represent the overwhelming majority of these observations. We build a model for the population of the BBHs based on the observed distribution of metallicities in galaxies and state-of-the-art stellar evolution models implemented through the Stellar EVolution N-body (SEVN) code. We calculate the primary mass spectrum and merger rates of BBHs and find general agreement with the redshift evolution and mass ratio distribution inferred by the LVK collaboration. When comparing to the primary mass distribution, our results indicate that either the average IMF in dwarf galaxies must be top heavy, or most of the 30 – 40 M_{\odot} black holes must be formed through a dynamical capture mechanism. For masses greater than about 50 M_{\odot} , the predicted number of BBH systems plummet to zero, revealing the well-known mass gap due to the pair instability mechanism and the mass loss in binary systems. We estimate the probability needed to fill part of the mass gap with mergers of dynamically-formed BBHs originating from the single black hole population.

Keywords: Gravitational wave sources(677) — Gravitational waves(678) — Black holes(162) — Stellar mass black holes(1611) — Compact objects(288)

1. INTRODUCTION

In 2015, the LIGO collaboration discovered the first direct evidence for gravitational waves (GWs) with the detection of event GW150914 (Abbott et al. 2016). Currently there have been three observing runs carried out, totaling 90 confirmed GW events, detected by the LIGO–Virgo–KAGRA (LVK) collaboration (The LIGO Scientific Collaboration et al. 2019; Abbott et al. 2021a; The LIGO Scientific Collaboration et al. 2021). Among the GW events are binary neutron star (BNS), neutron star–black hole (NS–BH), and binary black hole (BBH) mergers encompassing a wide mass spectrum.

These GW observations have revolutionized our understanding of compact objects. Prior to the first GW observation, the consensus was that black holes rarely exceeded $\gtrsim 20 M_{\odot}$ (Farr et al. 2011; Ozel et al. 2010). However, this perspective was challenged by the detection of GW150914, which featured component masses of 35.6 M_{\odot} and 30.6 M_{\odot} (Abbott et al. 2016). This landmark observation challenged existing assumptions and set forth a re-evaluation of black hole formation theories. Subsequent merger events have continued to challenge the field’s theoretical assumptions.

Two notable examples of changing perspectives are related to the so-called mass gaps in the compact object mass spectrum. The first mass gap, the *lower-mass gap*, occurs between the highest-mass neutron stars and the lowest-mass black holes. Neutron stars have long had a theoretical upper limit of $\sim 2.2 M_{\odot}$, termed the Tolman–Oppenheimer–Volkoff (TOV) limit (Bombaci 1996; Kalogera & Baym 1996; Rezzolla et al. 2018). Likewise, black holes were previously thought to only form down to a lower limit of $\sim 5 M_{\odot}$ (Farr et al. 2011), possibly resulting from core-collapse supernova physics (The LIGO Scientific Collaboration et al. 2022). This gap was postulated due to the dearth of observations of black holes below this threshold. Gravitational wave events GW 190814 (Abbott et al. 2020b), GW 200115 (The LIGO Scientific Collaboration et al. 2021; Abbott et al. 2021b), and a first result of the O4 run (Abac et al. 2024), along with the X-ray binary observation of ‘The Unicorn’ (Jayasinghe et al. 2021), among others, directly challenge the lower-mass gap expectation.

The second mass gap is predicted by the pair instability mechanism (Fowler & Hoyle 1964; Barkat et al. 1967; Fryer et al. 2001; Belczynski et al. 2016; Woosley et al. 2007; Woosley 2017, 2019), termed the *pair-instability mass gap* or the *upper-mass gap*. When a star’s core temperature reaches $\sim 10^9$ K the high-energy photons gain sufficient kinetic energy to annihilate into electron-positron pairs. This conversion reduces the radiation pressure of the star inducing gravitational collapse, leading to ignition of explosive oxygen/silicon burning. For helium core masses $30 \lesssim M_{\text{He}}/M_{\odot} \lesssim 60$ the core contracts and ignites burning, but it is not sufficient to completely disrupt the star. The star expands and cools to equilibrium, and this process can repeat leading to a series of pulsations lasting from a few hours to $\sim 10,000$ years (Woosley 2017). For higher mass cores $60 \lesssim M_{\text{He}}/M_{\odot} \lesssim 130$ the explosion disrupts the entire star, resulting in a pair-instability supernova with no remnant. For core masses exceeding this limit, $M_{\text{He}} \gtrsim 130 M_{\odot}$, the star collapses directly to a black hole as a result of the pair instability (Heger et al. 2003).

These examples highlight the increasing discrepancy between current theoretical expectations and observations. As gravitational wave observatories continue to get more data, hundreds more are predicted for observing run 4 (Broekgaarden et al. 2024). The new data will shed light on these compact objects and may also present new challenges for understanding their nature and origin. In light of this, it is imperative to develop sophisticated models that detail the formation and evolutionary pathways of these compact objects, particularly in the context of mergers.

In this study, we specifically focus on binary black hole systems that form and evolve through the isolated channel. This pathway consists of binary systems where the component stars interact with each other before merger but have negligible interaction with external pairs or the environment (García et al. 2021; Broekgaarden et al. 2021; Boesky et al. 2024a). In contrast, the dynamical channel involves interactions among single or multi-star systems within densely populated stellar environments, such as globular clusters, nuclear star clusters, or young star clusters (Sedda et al. 2023; Gerosa & Fishbach 2021; Mapelli et al. 2021; Farr et al. 2017). In the dynamical channel, stars frequently engage in close encounters or exchanges, leading to a series of complex dynamical interactions.

We show that we can obtain the LVK mass and redshift distributions by combining known galactic relationships, supported by observational evidence, and stellar evolution theory via the use of the Stellar EVolution N-body code called SEVN (Spera et al. 2015; Spera & Mapelli 2017; Spera et al. 2019; Mapelli et al. 2020), which utilizes the PARSEC tracks (Bressan et al. 2012; Tang et al. 2014; Chen et al. 2015; Marigo et al. 2017; Nguyen et al. 2022). We combine the metallicity distribution function (MDF) and the initial mass function (IMF) normalized by the average core-collapse supernova (CCSN) rate to estimate the average population of black holes per galaxy of a given stellar mass. Using the galactic stellar mass function (GSMF), we calculate the global number density of black holes and evolve it over time by incorporating the star formation rate (SFR) density and delay time distribution (DTD). This results in the merger rate density, which we directly compare to current gravitational wave observables.

Our paper is structured as follows. In Section 2.1, we begin by discussing the simulations used to inform and constrain our analysis. Following this, we construct the population of black holes in Section 2.2. The calculation of the merger rate density is detailed in Section 2.3. In Section 3, we compare the results of our model to those of the LVK collaboration. We conclude in Section 4.

2. METHODOLOGY

2.1. Zero-Age Main Sequence to Compact Object Evolution with SEVN Simulations

The first ingredient to properly model the binary black hole population is stellar evolution theory. To encapsulate the complex and broad physical processes involved in stellar evolution, we use the SEVN stellar evolution code (Spera et al. 2015; Spera & Mapelli 2017; Spera et al. 2019; Mapelli et al. 2020) to evolve stars from their zero-age main sequence (ZAMS) masses to their final remnant masses, including binary mergers. We evolve 1.4×10^9 binary configurations spanning the metallicity range $-3.1 \leq \log_{10}(Z/Z_{\odot}) \leq 0.2$ (18 logarithmically spaced bins) and uniformly sample progenitor masses in the range $10 \leq M/M_{\odot} \leq 200$ with a spacing of $1 M_{\odot}$.

We set the lower bound of our progenitor mass sampling to include progenitors that could potentially yield black holes. While the minimum mass for a single star to produce a black hole is $\sim 20 M_{\odot}$, binary interactions allow some progenitor stars with initial masses as low as $\sim 10 M_{\odot}$ to accrete enough material from their companions to collapse into black holes.

To obtain a representative sample of binary systems, following the sampling of M_1 and $\log_{10} Z$, we sample the mass ratio, eccentricity, and period from distributions following the results in (Sana et al. 2012) which are restated here for convenience:

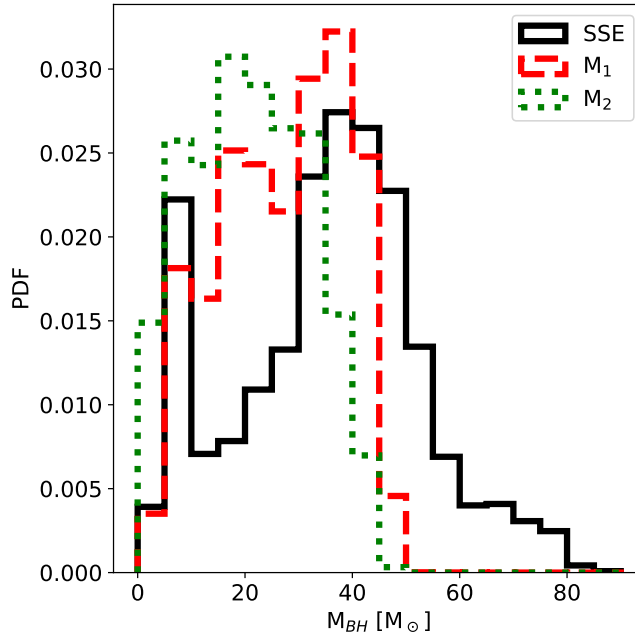


Figure 1. Distribution of black hole masses derived from binary and single stellar evolution using *SEVN*, with a bin size of $5 M_{\odot}$. The black dashed line represents black holes formed through single stellar evolution (SSE), while the red dashed line corresponds to the primary black hole in each surviving binary system. The green dotted line depicts the secondary black hole in each surviving binary system. This comparison highlights differences in the mass distribution for single stars versus binaries, emphasizing the role of binary interactions in shaping the population of black hole masses.

$$P(q_{ZAMS}) \propto q_{ZAMS}^{-0.1}, \quad q_{ZAMS} = \frac{M_2}{M_1}, \quad q_{ZAMS} \in [0, 1], \quad (1a)$$

$$P(\mathcal{P}) \propto \mathcal{P}^{-0.55}, \quad \mathcal{P} = \log_{10}(\text{P/day}), \quad \mathcal{P} \in [0.15, 5.5], \quad (1b)$$

$$P(e) \propto e^{-0.42}, \quad e \in [0, 0.9]. \quad (1c)$$

In our model, we assume zero initial spins for the progenitor stars. This assumption is well justified, as the majority of the star’s primordial angular momentum is lost during its evolution due to Roche-lobe overflow mass transfer and wind mass loss (Qin et al. 2018; Bavera et al. 2020). These studies show that as the star expands, its angular momentum is transferred to the outer layers, which are subsequently removed through the aforementioned processes. Specifically, Bavera et al. (2020) highlight that the initial angular momentum is mostly lost by the time a star becomes a helium star, and Qin et al. (2018) emphasize that most of the angular momentum a star might have had is lost during this expansion phase, making the initial spin largely irrelevant for the final spin of the black hole. By assuming zero initial spin, we have simplified the model without sacrificing accuracy, as the black hole’s spin is dominated by processes such as mass transfer, tidal synchronization, and accretion in the binary system’s later evolutionary stages.

Only binary systems that contain two black holes and merge within a Hubble time (~ 14 Gyr), are included in the analysis. We show the distributions for the primary and secondary masses from our binary stellar evolution (BSE) runs, coupled with the single stellar evolution (SSE) distribution in Figure 1. The black solid histogram is for SSE case where $M_{1,max}^{SSE} \sim 90 M_{\odot}$; there is a narrow peak at $\sim 20 M_{\odot}$ (arising from CCSN physics) and a wider peak at $\sim 40 M_{\odot}$ indicating a build-up due to the pair instability mechanism. The red dashed histogram is the primary black hole from our evolved simulations with $M_{1,max}^{BSE} \sim 80 M_{\odot}$, but with a significant drop in statistics at $\sim 50 M_{\odot}$ due to the pair instability mechanism. The green dotted histogram in Figure 1 is for the secondary black hole masses of the binary systems with a maximum of $M_{2,max}^{BSE} \sim 45 M_{\odot}$.

Each of these black holes can have a range of progenitor masses that have undergone varying degrees of mass evolution due to intrinsic stellar processes and binary interactions. Before we fold in galactic dynamics for a full

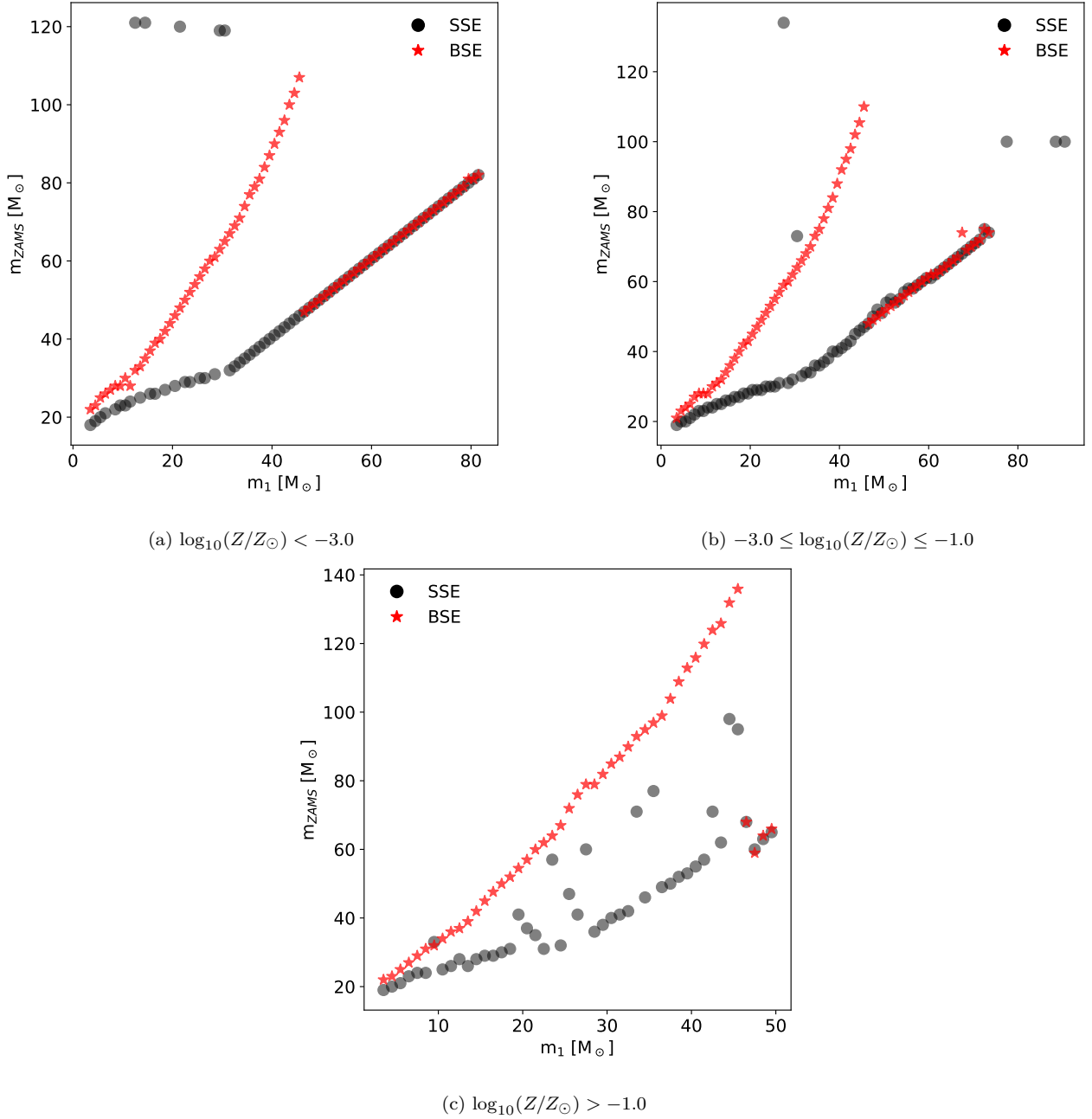


Figure 2. This figure shows the median progenitor mass required to form a primary black hole for both BSE and SSE scenarios across three different metallicity regimes. In the SSE case, higher metallicity systems exhibit a broader spread, attributed to reduced statistics due to fewer black holes being formed. For the BSE case, the evolutionary track diverges from the SSE track up to $\sim 50 M_\odot$. Beyond this point, stars in binaries that merge within a Hubble time typically evolve with minimal disruption, eventually forming remnants that realign with the SSE track. Such systems are exceptionally rare.

population analysis, we estimate the typical progenitor mass for each black hole based on the distributions in Equation 1. We compare the results of the SSE and BSE models by categorizing them into three distinct metallicity regimes: low ($\log_{10}(Z/Z_\odot) < -1.5$), medium ($-1.5 \leq \log_{10}(Z/Z_\odot) \leq -0.5$), and high metallicity ($\log_{10}(Z/Z_\odot) > -0.5$). The median black hole mass as a function of progenitor mass is shown in Figure 2. Systems with higher metallicities tend to exhibit a wider spread in M_{ZAMS} for the SSE case. This broadening results from the lower probability of forming black holes at higher metallicities, which reduces statistics and increases variability. The impact of binary interactions

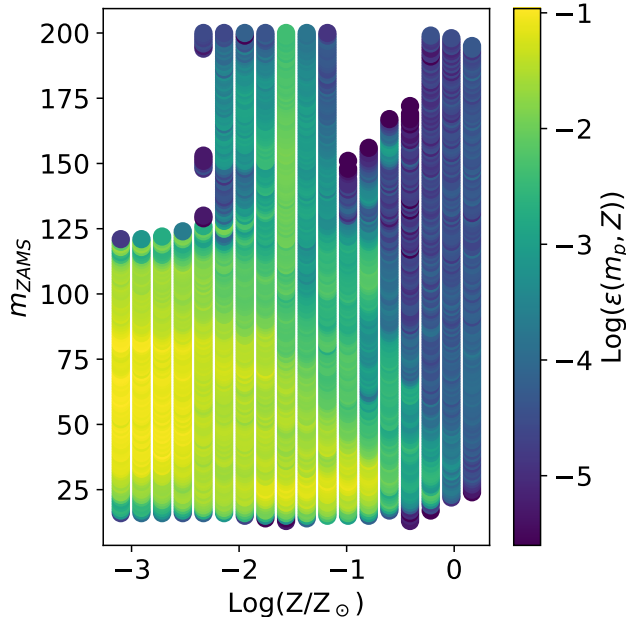


Figure 3. The efficiency for black holes to form in each metallicity bin color coded by progenitor mass, M_{ZAMS} . Low-metallicity progenitors exhibit a higher efficiency and overall survivability probability. In contrast, higher-metallicity systems, although they may avoid pair instability, have a much lower probability of survival as indicated by the reduced efficiency factor.

is evident in the BSE data, with a notable peak in the median progenitor mass for black holes of $\sim 50 M_{\odot}$. This peak corresponds to the threshold where the pair instability process becomes dominant, effectively capping the mass of black holes formed from more massive stars. Beyond this point, the paths for BSE and SSE models converge, reflecting the scenarios where binary stars evolve almost independently, mirroring the solitary evolution of SSE. While these systems are exceptionally rare, there are a few that manage to merge within a Hubble time.

Both $M_{1,max}^{SSE}$ and $M_{1,max}^{BSE}$ reside within the pair-instability mass gap, as such their production is expected to be highly suppressed (Fowler & Hoyle 1964; Barkat et al. 1967; Fryer et al. 2001; Belczynski et al. 2016; Woosley et al. 2007; Woosley 2017, 2019), yet the LVK collaboration has reported several events within this gap (Abbott et al. 2020c,d; The LIGO Scientific Collaboration et al. 2021). These massive black holes form in the SEVN code as the remnants of low-metallicity progenitor stars of $\sim 100 M_{\odot}$, and avoid the pair instability mechanism during their late dredge-up phase as the mass of the helium core is reduced to just below the threshold required for PISN, $\sim 32 M_{\text{He}}$ (Spera et al. 2019). The star can then end its life with roughly the mass at the end of helium depletion phase, producing a massive BH that lies in the pair-instability mass gap. While these kinds of black holes do form in SEVN, they are exceptionally rare and predictions for black holes with masses above $\sim 50 M_{\odot}$ should be interpreted with care.

The evolutionary dynamics of binary evolution are further illustrated in Figure 4 for 10 different metallicities. The red dashed line in each plot represents the evolutionary track of single stars; in this case, each progenitor and metallicity combination produces a unique black hole mass. In contrast, the BSE model exhibits a wide range of black hole masses for each progenitor mass-metallicity combination. Each subplot represents the BSE case through hexagonal binning, each bin with a width of $2 M_{\odot}$, and the colorbar logarithmically represents the density. As mentioned above, the behavior of systems with progenitor masses exceeding $\sim 50 M_{\odot}$ aligns with the SSE path, which implies relatively isolated evolution within the binary system. Note that these are statistically insignificant when compared to the total population. The number of surviving systems that form a BBH pair and merge within a Hubble time shows a large variation, ranging from $\sim 3 \times 10^6$ for the lowest-metallicity systems to $\sim 2 \times 10^3$ in the highest-metallicity systems. Interestingly, for intermediate metallicities, $-2.0 \lesssim \log_{10}(Z/Z_{\odot}) \lesssim -0.75$, there exists a region where progenitor masses that would otherwise not form black holes under SSE conditions can form black holes in the BSE scenario due to mass transfer between the system. Lastly, for the most metal-rich systems, the evolutionary path follows the

SSE case, which could be due to intense stellar winds disrupting binary systems and leaving only those that evolve in relative isolation.

It is clear that the mass distribution of surviving binary black hole masses is intricately shaped by the progenitor characteristics and the orbital configurations of each system. To accurately capture this complex relationship, we introduce an efficiency parameter, $\varepsilon(M_p, Z)$. This parameter represents the likelihood of a star, for a given progenitor mass and metallicity, to form a black hole of any mass, marginalized over the orbital parameters. This efficiency factor is defined as:

$$\varepsilon(M_p, Z) = \frac{\mathcal{N}_{\text{sur}}(M_p, Z)}{\mathcal{N}_{\text{sim}}(M_p, Z)}, \quad (2)$$

where $\mathcal{N}_{\text{sur}}(M_p, Z)$ represents the number of primary binary black hole progenitors that successfully merge within a Hubble time as determined from our sampling, and $\mathcal{N}_{\text{sim}}(M_p, Z)$ denotes the total number of simulated progenitor configurations. The results from Equation 2 are depicted in Figure 3. This figure clearly demonstrates that stars with lower metallicity have a higher likelihood to form black hole remnants, consistent with recent findings by (Schiebelbein-Zwack & Fishbach 2024). While the efficiency factor for creating black holes in general is higher at lower metallicities, these metallicities are less frequently observed in nature, and the progenitors are also more likely to undergo pair-instability supernova as indicated by the dip in the maximum M_{ZAMS} for black holes at $\log_{10}(Z/Z_{\odot}) \lesssim -2.5$.

We construct the joint distribution of the primary black hole mass and mass ratio, $p(M_1, q | M_p, Z)$, derived from the population of surviving binary black hole systems. For each combination of progenitor mass M_p and metallicity Z , we use a two-dimensional kernel density estimate (KDE) over the M_1 - q space to determine the density. The resulting joint distribution $p(M_1, q | M_p, Z)$ is then normalized by our efficiency function from Equation 2. Finally, we interpolate the normalized distribution bilinearly over a grid of Z and M_p values, ensuring full representation across the parameter space.

2.2. Galactic Binary Black Hole Population

Utilizing the results from Section 2.1, we develop a comprehensive model of the binary black hole population per galaxy, building on the formalism introduced in (Elbert et al. 2018). The focus is on the primary black holes within each binary system, with the intention of comparing to observational data from the LVK collaboration. Our model is founded on fundamental assumptions about the astrophysical processes governing galaxies, where massive stars evolve into black holes. We incorporate essential galactic relations, including the MDF and IMF. The MDF provides insights into the relationship between galaxy mass and metallicity, while the IMF describes the distribution of stellar masses within a galaxy.

By convolving these empirical relations, with the joint distribution of primary masses and mass ratios from our simulations, $p(M_1, q | M_p, Z)$, integrated over q , we obtain the differential number of binary black holes as a function of galaxy mass. This approach allows us to analyze how galactic properties influence the primary mass function in binary black hole systems, offering a detailed understanding of their formation and evolution across varying galactic environments. The population is described by the following integral:

$$\frac{dN_{BBH}}{dM_1}(M_*) = C_N \int_{q_l}^{q_u} \int_{Z_l}^{Z_u} \rho(Z | M_*) \int_{8M_{\odot}}^{M_u} \left(\frac{M_p}{M_{\odot}}\right)^{\alpha} p(M_1, q | M_p, Z) dZ dq d\left(\frac{M_p}{M_{\odot}}\right). \quad (3)$$

The distribution function of primary black holes, $p(M_1, q | M_p, Z)$, is calculated as given in Section 2.1, normalized by $\varepsilon(M_p, Z)$ defined in Equation 2. The MDF, $\rho(Z | M_*)$, is assumed to follow a log-normal distribution within the limits defined by the range $-3.0 < \log_{10}(Z/Z_{\odot}) < 0.5$. We verified that extending the integral limits to $-4.0 < \log_{10}(Z/Z_{\odot}) < 1.0$ yields only negligible differences. The mean and variance, $\mu(M_*)$ and $\sigma(M_*)$, are obtained from observational surveys (Gallazzi et al. 2005; Kirby et al. 2013; Kirby et al. 2017; Koposov et al. 2018, 2015; Simon et al. 2015; Li et al. 2017; Fabrizio et al. 2012; Li et al. 2018; Frebel et al. 2014; Willman et al. 2011; Collins et al. 2017; Caldwell et al. 2017; Kirby et al. 2015; Ji et al. 2016; Brown et al. 2014; Longeard et al. 2018; Mucciarelli et al. 2017; Kim et al. 2016; Chiti et al. 2018; Walker et al. 2016; Simon et al. 2017; Simon 2019). For the dwarf galaxy Willman I, there is no value quoted for the dispersion in the MDF. We use $\sigma(M_*) = 0.4$, as this is a common value among similar galaxies. We fit a univariate spline of polynomial order 3 to the data points, which we interpolate over the given values for our integration across the MDF as shown in Figure 5. Lastly, the q integral is over the range given by: $q_l = 0.0, q_u = 1.0$.

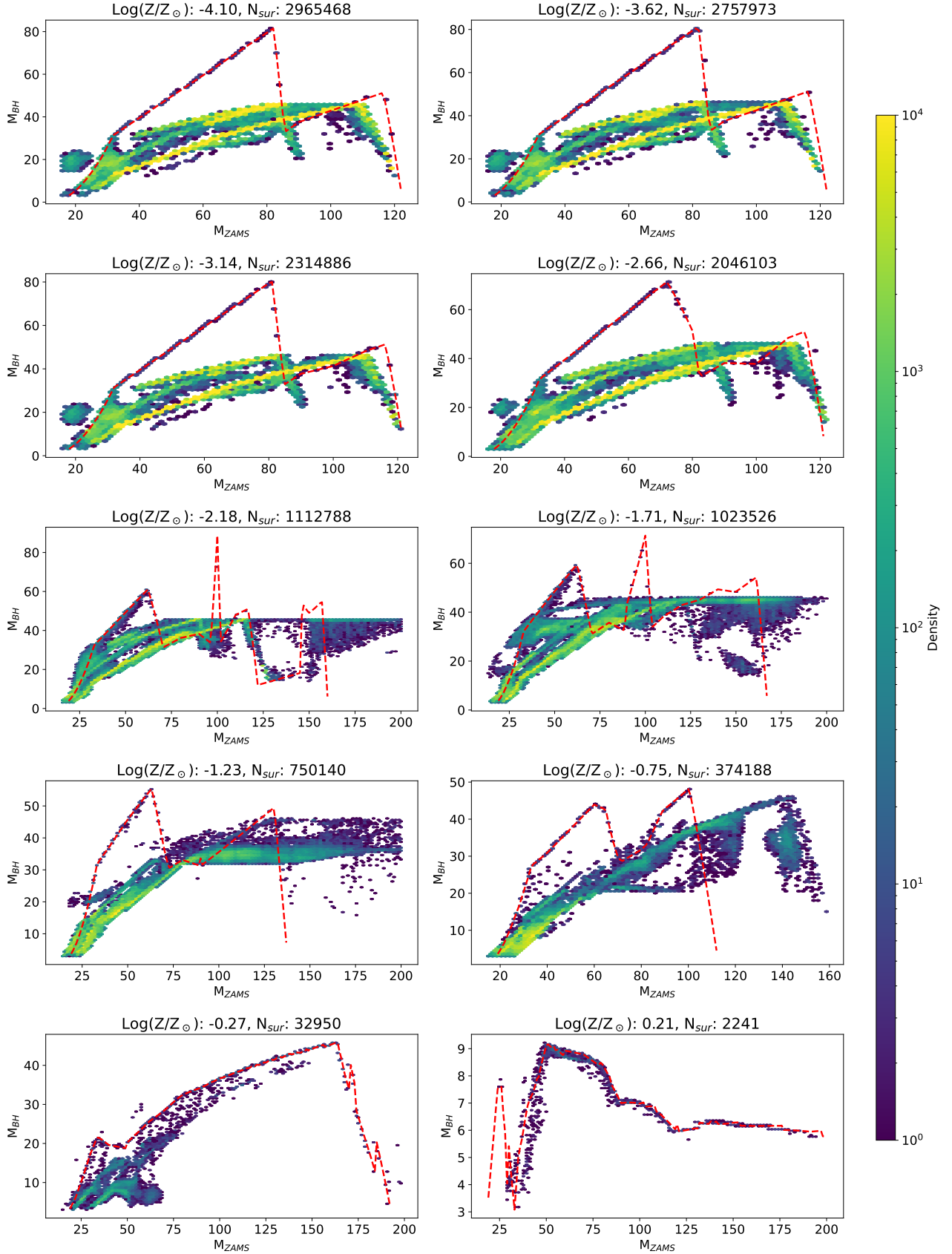


Figure 4. Density plots of the primary ZAMS mass versus BH mass across different metallicities. The title of each plot indicates the unique metallicity and the number of surviving systems, highlighting the substantial variations across the metallicity range. The density of points is visualized using hexagonal binning, with each bin spanning $2 M_{\odot}$, and the color intensity represents the logarithmic density of points. The red dashed lines depict the evolutionary tracks from the single stellar evolution model.

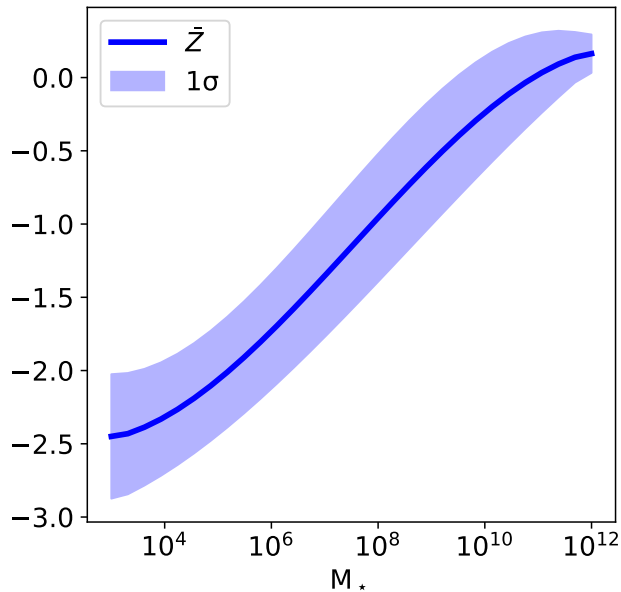


Figure 5. Our fit for the metallicity distribution function as a function of galaxy mass, based upon observations from Gallazzi et al. (2005); Kirby et al. (2013); Kirby et al. (2017); Kaposov et al. (2018, 2015); Simon et al. (2015); Li et al. (2017); Fabrizio et al. (2012); Li et al. (2018); Frebel et al. (2014); Willman et al. (2011); Collins et al. (2017); Caldwell et al. (2017); Kirby et al. (2015); Ji et al. (2016); Brown et al. (2014); Longeard et al. (2018); Mucciarelli et al. (2017); Kim et al. (2016); Chiti et al. (2018); Walker et al. (2016); Simon et al. (2017); Simon (2019). The solid line represents the mean metallicity, while the shaded region indicates the 1σ uncertainty band.

We adopt the ansatz that the stellar population follows a power-law distribution, M_p^α , for the initial stellar mass function over the relevant progenitor mass range that leads to black hole remnants. This distribution, derived from the initial mass function (IMF), quantifies the relative frequency of star formation as a function of mass, for black hole progenitors. To account for the possibility of a top-heavy IMF, we allow the exponent α to change as a function of stellar mass using the relation $M^{-2.3+\beta \log_{10}(M_p/8)}$, which we refer to as our running-slope model. Here, β sets the stellar mass-dependent flattening or steepening of the IMF. We use a value of $\beta = 0.7$ to introduce a gradual flattening of the IMF at higher masses, enhancing the high-mass black hole population synthesis without overshooting it.

In this work, we present results based on two IMFs, the constant slope of -2.3 (i.e., $\beta = 0$) consistent with the Kroupa IMF (Kroupa 2001) and the running-slope model with $\beta = 0.7$. Note that we choose a slope of -2.3 at $8 M_\odot$ for both models to facilitate comparison between the two models. We have not performed a scan of parameters to determine what would best fit the LIGO data, as this exercise would be premature given the uncertainties that still need to be explored. This comparison also highlights the potential impact of metallicity-driven variations of the IMF, the black hole mass distribution, and the number density. There is evidence suggesting potential variations at the high-mass end due to environmental factors such as metallicity in dwarf galaxies and globular clusters (Geha et al. 2013; Gennaro et al. 2018; Marks et al. 2012; Weatherford et al. 2021).

To normalize the distribution, we require a measure that is sensitive to the subset of stars in this mass range, rather than the entire stellar mass population or star formation history, which would include contributions from lower-mass stars that do not result in black holes. A natural choice for this normalization is the specific CCSN rate, \mathcal{S}_{CCSN} , as it effectively captures the majority of black hole progenitors in the galaxy. The Lick Observatory Supernova Search (Li et al. 2011) derived a power-law dependence for the specific CCSN rate today, $\mathcal{S}_{CCSN} \propto M^{-0.55 \pm 0.1}$, based on observations of galaxies with $M_* \gtrsim 10^9 M_\odot$. However, massive galaxies experience most of their star formation, and thus CCSNe, early in their history, which would create a mass dependence in the CCSN rate today. In addition, extrapolating this power-law behavior to lower galaxy masses would be at odds with the SFR for the fainter galaxies Johnson et al. (2013) unless there the IMF was adjusted, suggesting that the specific CCSN rate should become

constant for $M_\star \lesssim 10^9 M_\odot$. A more detailed modeling of the CCSN rate (along the lines of our BBH population modeling) would be useful here.

Here, we adopt a simplified average specific CCSN rate, $\bar{\mathcal{S}}_{CCSN}$, as a constant normalization factor. This rate represents a time-averaged CCSN rate over cosmic history, effectively approximating the total number of CCSNe over a galaxy's lifetime. The normalization can be expressed as:

$$C_N \int_{8M_\odot}^{M_u} \left(\frac{M_p}{M_\odot}\right)^\alpha d\left(\frac{M_p}{M_\odot}\right) = \bar{\mathcal{S}}_{CCSN}(M_\star) \times M_\star \times f_{\text{bin}} \times (1/2) \times (13.7 \text{ Gyr}). \quad (4)$$

On the RHS of Equation 4 $\bar{\mathcal{S}}_{CCSN}$ is treated as constant across galaxy masses. We use a value of $\bar{\mathcal{S}}_{CCSN} = 1.5 \times 10^{-12} \text{ yr}^{-1} M_\odot^{-1}$ to best align our model with LVK observations of BBH mergers. For reference, the specific CCSN rate from the Lick observations for galaxies with stellar mass of $10^9 M_\odot$ is about $2 - 3 \times 10^{-12} \text{ yr}^{-1} M_\odot^{-1}$ (including Type II and Type Ibc). This implies that we are unlikely to be overestimating the CCSN rate.

We can also verify this against the predicted CCSN for typical IMFs. For example, if we assume that $\alpha = -2.3$ for $1 < M_p/M_\odot < 8$, $\alpha = -1$ for $0.1 < M_p/M_\odot \leq 1$ and our running model with $\beta = 0.7$ for $M_p > 8 M_\odot$, we find specific age times CCSN rate (obtained by integrating the IMF from $8 - 200 M_\odot$) is $0.015 M_\odot^{-1}$. This value does not change significantly for the $\beta = 0$ model, as expected. For an age of 10 Gyr, this value is consistent with the specific CCSN rate we assumed. This serves as another consistency check for the CCSN rate used in our model.

The upper bound on the integral, M_u , is chosen to be $M_u = 200 M_\odot$ rather than the Eddington limit, in light of the various stars observed with estimated masses greater than $150 M_\odot$ (Crowther et al. 2010; Bestenlehner et al. 2014, 2020). We note that, due to the suppression by the IMF, this change in limits has a negligible impact on the overall result. The factor of 1/2 in Eq. 4 is included to avoid double counting, as we are only considering the primary mass of the binary. The overall binary fraction of stars in the galaxy is denoted by f_{bin} .

The study by Sana et al. (2008) finds the intrinsic binary fraction to be $f_{\text{bin}} \sim 0.7$, while Moe & Di Stefano (2017) report that O-type stars are more commonly found in triples ($n = 3$) and quadruples ($n = 4$), with $f_{n \geq 3} = 0.73$ and $f_{\text{bin}} = 0.21$. Triples and quadruples contributing to the merger rate would consist of a closer-orbit binary pair with additional stellar companions. While we do not explicitly factor in $n \geq 3$ systems, our model accounts for a subset of their evolution. Thus, $f_{\text{bin}} \in [0.21, 0.94]$. For consistency with both studies, we adopt $f_{\text{bin}} = 0.7$ throughout.

2.3. Evolution in Space and Time

We now have a prediction for the population of black holes for a given galaxy mass, dictated by galactic relations and stellar evolution theory implemented in the SEVN simulations. Our focus is on the number of black holes formed that would merge within a time frame suitable for the observation of their gravitational wave signatures. To extend this analysis from individual galaxies to a volumetric population, we integrate Equation 3 over the galaxy stellar mass function (GSMF), $\phi(M_\star)$, which quantifies the number of galaxies per unit volume per dex of galaxy mass:

$$\frac{dn_{BBH}}{dM_1} = \int_{M_{\text{min}}}^{\infty} \phi(M_\star) \frac{dN_{BBH}}{dM_1}(M_\star) dM_\star. \quad (5)$$

The shape of the GSMF is well-fit by the double-Schechter function from Baldry et al. (2012) and appears to remain constant to $z \sim 2$, beyond which a single Schechter function seems to be preferred (Weaver et al. 2023). Furthermore, Stefanon et al. (2021) find that for redshifts $z > 7$, the GSMF is better described as a power-law. For simplicity, we adopt the form detailed in Baldry et al. (2012) throughout our calculations. Figure 6 depicts the cumulative density of black holes per Gpc^{-3} . The blue lines represent the global number density of single black holes, while the black lines represent primary black holes in binary systems. The dotted lines correspond to α_{const} , while solid lines correspond to α_{run} , our constant- and running-slope model respectively.

There is a peak at $\sim 35 M_\odot$ in the SSE case, indicating a build-up due to the pair instability mechanism, which persists in the case of binary stellar evolution (BSE). Note how the SSE distribution is distorted and reduced due to binary interactions and the constraint on the merger time. For the SSE case, we observe some black holes in the upper mass gap, although their abundance drops sharply beyond the lower bound. For BSE, these black holes are almost entirely absent, with their numbers dropping by several orders of magnitude. Not only is mass-gap black hole formation rare in our model, but the efficiency with which they form in binary systems that successfully merge within a Hubble time is exceedingly low.

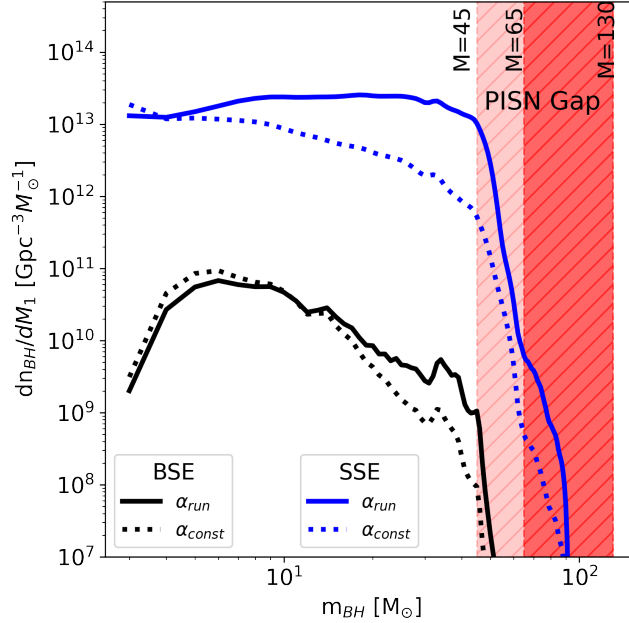


Figure 6. The global number density of black holes per unit volume. The blue lines correspond to the single stellar evolution (SSE) scenario, while the black lines represent the binary stellar evolution (BSE) scenario. For both SSE and BSE, solid lines depict results from the running-slope model ($\alpha_{\text{run}} = -2.3 + \log_{10}(M/8M_{\odot})\beta$), with $\beta = 0.7$, and dotted lines show results from the constant-slope model ($\alpha_{\text{const}} = -2.3$). A peak at $M_{\text{BH}} \sim 35 M_{\odot}$ appears in both SSE and BSE, driven by remnant build-up from the pair instability mechanism. Additionally, an extra build-up at $M_{\text{BH}} \sim 15 M_{\odot}$ emerges in the BSE case due to binary interactions. At the lower end of the BSE spectrum, a natural tapering is visible, caused by binary effects and the reduced prominence of primary black holes at lower masses.

Using this formalism, we can determine the likelihood of black hole formation within various galaxies and their corresponding mass ranges. Figure 7 highlights the differences between the BSE and SSE pathways. Both exhibit a marked decline in black hole formation above $\sim 50 M_{\odot}$, although the decrease is more pronounced in the BSE case due to binary interactions. The distinct characteristics of the SSE and BSE populations highlight the importance of incorporating binary effects in models to properly align with observational data from the LVK collaboration. The most interesting feature in Figure 7 is that for masses above about $30 M_{\odot}$, most of the BBH are formed in dwarf galaxies. As shown, for $45 M_{\odot}$ the most likely hosts are galaxies with stellar masses of about $10^7 M_{\odot}$.

The final ingredient in our model is temporal evolution. To accurately predict the merger rate density inferred by the LVK collaboration, we must determine the rate at which stars form, collapse to black holes, and subsequently merge. To capture the star formation rate, we use the parameterization from Madau & Fragos (2017). We note that this remains an area of significant activity, necessitating further investigation (Boesky et al. 2024a,b). The resulting birth rate for binary black holes takes the following form:

$$\frac{d\dot{n}_{\text{BBH}}}{dM_1}(t) = \frac{dn_{\text{BBH}}}{dM_1} \frac{\psi(t)}{\int_0^{t_0} \psi(t) dt}. \quad (6)$$

The delay between the formation and merger of binary black holes, τ , depends on the orbital parameters and the mass-loss history. We calculate the delay-time distribution (DTD), $P(\tau)$, directly from our simulations, as shown in Figure 8. Due to the high mass of the stars that we consider, their average lifetimes are negligible in comparison to the DTD. We fit a power-law function of the form $P(\tau) \propto \tau^{-0.85}$ to the DTD and use that function in the integral. After integrating over the DTD, we arrive at the differential merger rate:

$$\frac{d\mathcal{R}}{dM_1} = \int_0^{t_0} \frac{d\dot{n}_{\text{BBH}}}{dM_1}(t_0 - \tau') P(\tau') d\tau'. \quad (7)$$

3. RESULTS

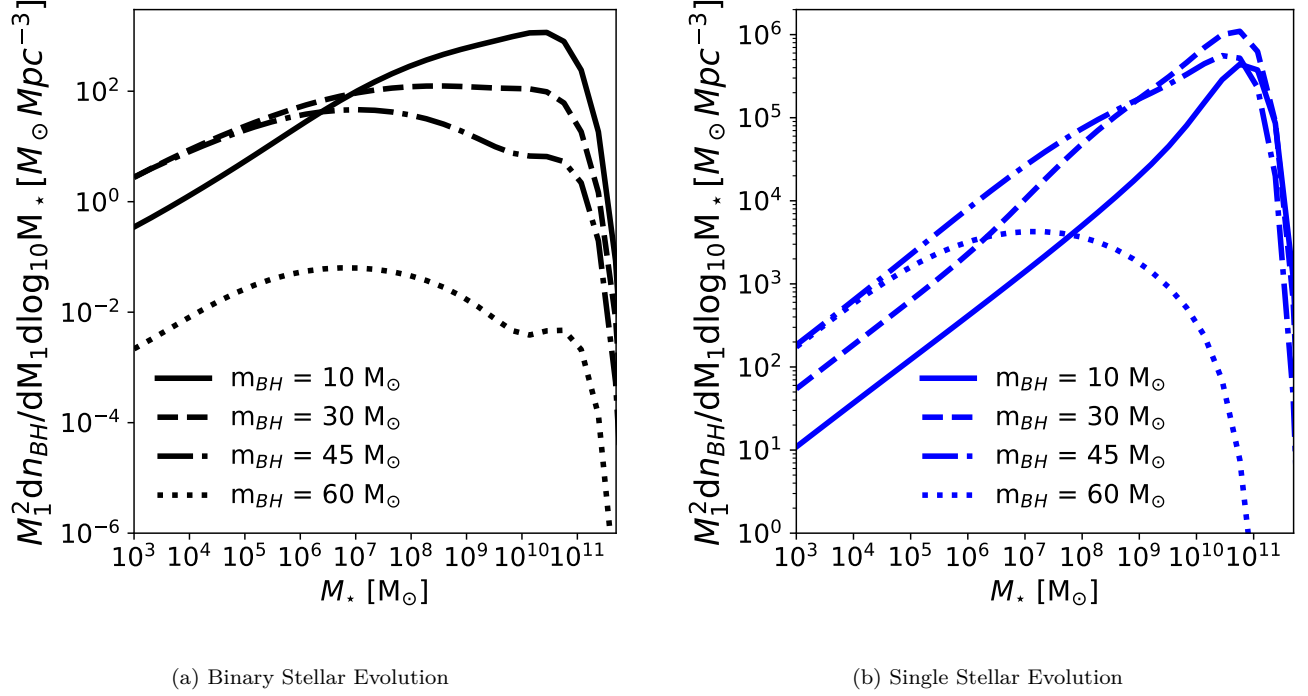


Figure 7. Differential number density of black holes as a function of galaxy mass. *Left panel:* The BSE model shows a significant decline in the number density of black holes beyond a threshold of $50 M_{\odot}$, reflecting the upper mass limit imposed by the pair instability mechanism. *Right panel:* The SSE model reveals a significantly higher abundance of black holes across all masses, compared to the BSE scenario.

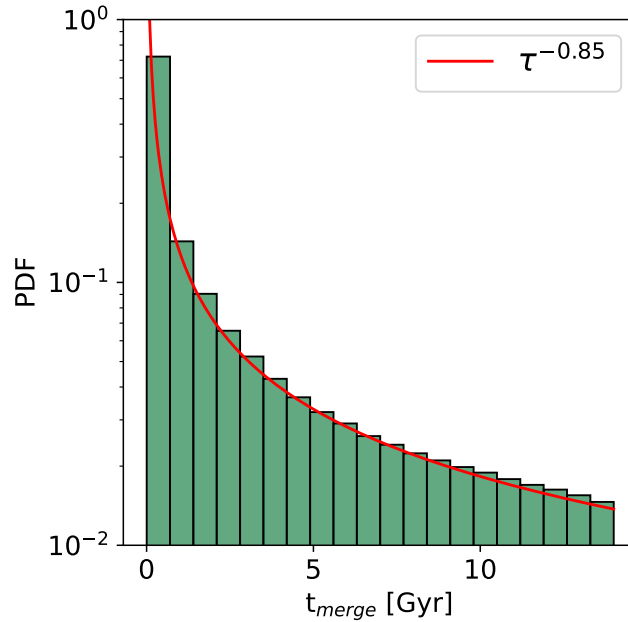


Figure 8. Power-law fit to the merger time distribution from the SEVN simulations. As we consider very high-mass stars, their lifetimes are $\ll 1$ Gyr and negligible compared to the delay-time distribution (DTD). Thus, this distribution can be directly used as the DTD in Equation 6.

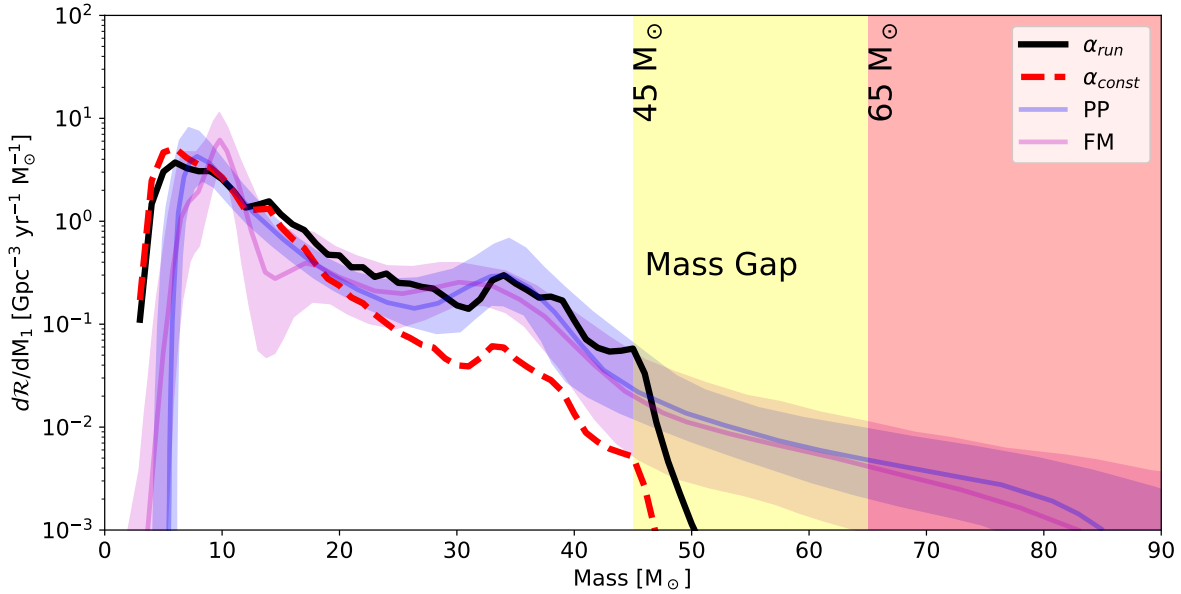


Figure 9. Comparison between the LIGO-Virgo-KAGRA *power-law + Peak (PP)* and *Flexible Mixtures (FM)* models, depicted in blue and magenta, respectively, and our models: the constant-slope IMF ($\alpha = -2.3$, red dashed line) and the running-slope IMF ($\alpha = -2.3 + 0.7 \log_{10}(M/8M_{\odot})$, black solid line). The peak at $\sim 35 M_{\odot}$ is less pronounced in the constant-slope model but is corrected by adopting a top-heavy IMF in the running-slope model. We obtain very few BBH mergers in the pair-instability mass gap, consistent with standard stellar theory. This is reflected by the truncation of our model around $\sim 50 M_{\odot}$. The conservative pair-instability supernova (PISN) gap bound is indicated by the yellow band at $45 M_{\odot}$, while the optimistic bound is shown by the red band at $65 M_{\odot}$.

3.1. Binary Black Hole Mass Spectrum

In the previous section, we discussed the calculation of the merger rate density given in Equation 7. Throughout this section, we compare our results to the gravitational wave observations from the LVK collaboration and find significant agreement with their findings. In the most recent gravitational wave transient catalog ([The LIGO Scientific Collaboration et al. 2021, 2022](#)), the LVK collaboration parameterizes the merger rate density using several comparative models, with the power-law + peak (PP) chosen as their fiducial model. This model follows a power-law with a Gaussian peak centered at $\sim 35 M_{\odot}$, along with a smoothing function that acts to smoothly turn off the spectrum at low masses.

In Figure 9, we compare the differential merger rate with respect to the primary mass of the binary system for our two models (see Section 3.1) at $z = 0.2$ with LVK’s PP and flexible mixture (FM) models. We find that the running-slope model exhibits greater agreement with their observations, suggesting that mass-dependent variations in the IMF, required mainly in dwarf galaxies, play a significant role in shaping the BBH mass distribution. The Gaussian component of their model, at $\sim 35 M_{\odot}$, is apparent in our model due to the aforementioned build-up from the pair instability mechanism ([Woosley & Heger 2015; Woosley 2017](#)). The smoothing function introduced in the LVK analysis is attributed to parameters such as metallicity, which blur the edge of the proposed lower mass gap ([Abbott et al. 2019](#)).

We find that, due to binary effects, our model naturally tapers off at lower masses. However, it is important to note that the exact location of the first peak following this tapering is slightly shifted in our analysis. This discrepancy arises from differences in the choice of the lowest black hole mass between our model and the LVK collaboration. In [The LIGO Scientific Collaboration et al. \(2022\)](#), the LVK collaboration uses $5 M_{\odot}$ as the lower bound, while we use $3 M_{\odot}$, as there is increasing evidence for objects in the proposed gap between the heaviest neutron stars and the lightest black holes.

Our model demonstrates good agreement with the observed differential merger rate across much of the primary mass spectrum, including the tapering at low masses and the peaks. However, discrepancies arise at the high-mass end of

the spectrum, where the model underestimates the number of binary black holes required to populate the observed tail of the merger-rate distribution. This suggests that black holes in this range may originate from an alternate population. Possible explanations for the high-mass tail of the distribution include population III stars (Farrell et al. 2021; Kinugawa et al. 2021; Liu & Bromm 2020), hierarchical mergers (Sedda et al. 2023; Gerosa & Fishbach 2021; Mapelli et al. 2021; Farr et al. 2017; Antonini et al. 2022; Torniamenti et al. 2024), primordial black holes (De Luca et al. 2021), or beyond the Standard Model (BSM) physics (Croon et al. 2020; Sakstein et al. 2020; Ziegler & Freese 2021, 2024; Croon & Sakstein 2024).

An intriguing avenue to explore the population of mergers within the upper mass gap lies in the role of single black holes. Although the fraction of massive stars born as singles is relatively low (around 10%), these single black holes evolve in isolation from ZAMS to BH and are not subject to the same efficiency factor constraints as shown in Figure 3. As a result, if they retain their hydrogen envelopes, they can form more massive black holes, even extending into the mass gap.

Once formed, single black holes can enter binaries through dynamical capture, a process that depends on several factors, including the cluster density, stellar interaction rates, and black hole retention within these environments. After formation, black holes tend to migrate toward the cluster core due to dynamical relaxation (Portegies Zwart & McMillan 2000). Closer to the cluster core, the more frequent dynamical encounters can result in the formation of binaries or higher-order systems. While many black holes will experience multiple interactions or even ejection from the cluster, some may successfully become part of a binary system capable of merging within a Hubble time.

We sketch a simplified picture to estimate the efficiency of this process, η , which we define as the probability for a single black hole to capture a companion (i.e., form a binary) and merge within the age of the universe. We can break up this efficiency into various factors to get a better idea; $\eta \sim f_{\text{sse}} \times f_{\tau} \times f_{\text{dyn}} \times f_{\text{GC}} \times f_{\text{primary}}$. Here, f_{sse} represents the fraction of massive stars born as singles, f_{τ} is the probability for dynamically formed binaries to merge within a Hubble time, f_{dyn} accounts for the fraction of dynamically interacting black holes that form binaries instead of being ejected that is likely dependent on metallicity (Kumamoto et al. 2020), f_{GC} quantifies the fraction of black holes residing in dense stellar environments like globular clusters (which we expect to be dependent on the stellar mass of the galaxy and perhaps its metallicity), and f_{primary} reflects the likelihood that the single black hole becomes the primary in the binary. These various factors depend on the mass of the single black hole, which would require detailed simulations to explore.

To explore the possibility of binaries formed dynamically contributing to the upper mass gap, we decompose the total differential merger rate into two components:

$$\frac{dR}{dM_1} = \frac{dR_{\text{BBH}}}{dM_1} + \bar{\eta}(M_1) \frac{dR_{\text{SBH}}}{dM_1}, \quad (8)$$

where $\frac{dR_{\text{BBH}}}{dM_1}$ corresponds to the contribution from black holes formed in isolated binaries, while $\frac{dR_{\text{SBH}}}{dM_1}$ accounts for the contribution from single black holes and $\bar{\eta}$ is the efficiency averaged over galaxy masses and metallicities. Given our discussion above, we should build in the efficiency calculation before averaging over the properties of galaxies but we are only interested in an order of magnitude answer here. If the black hole mass dependence of $\bar{\eta}$ is neglected, we can do a quick estimate of the efficiency needed to populate black holes in the mass gap. We estimate that, for an efficiency $\bar{\eta} \sim 10^{-4}$, the contribution from dynamically formed binaries can extend the black hole mass spectrum up to about $60 M_{\odot}$.

It is also worth keeping in mind that the lower mass when pair instability kicks in is not well known. The effects discussed in Woosley & Heger (2021) suggest that the pair instability could shift to higher masses ($\sim 65\text{--}70 M_{\odot}$) and this would offer an additional way to populate the mass gap. It would be interesting to include these effects along with the mass loss in binary systems to explore this further. Together, these considerations present pathways to populate the upper-mass gap that deserve further study.

3.2. Redshift Dependence

To obtain the total merger rate at a given redshift, we first determine dR/dM_1 at the corresponding cosmic time, $t_0 = t(z)$, using Equation 7. We then integrate over the black hole primary mass to find $\mathcal{R}(z)$:

$$\mathcal{R}(z) = \int \frac{d\mathcal{R}}{dM_1}(z) dM_1. \quad (9)$$

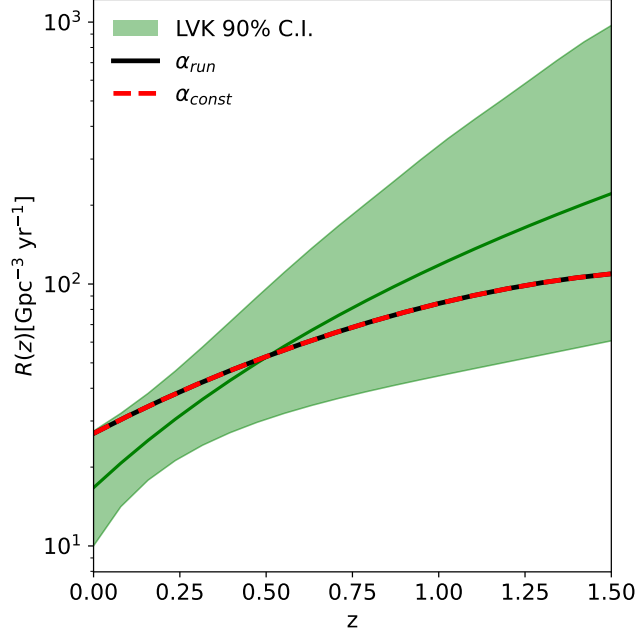


Figure 10. Comparison of the merger rate evolution with redshift for our constant- and running-slope models with the LVK’s inferred rate. The black line represents our running-slope model ($\alpha_{\text{run}} = -2.3 + \log_{10}(M/8M_{\odot})\beta$), with $\beta = 0.7$, as described in Section 3.1. The red dashed line represents our constant-slope model ($\alpha_{\text{const}} = -2.3$). For reference, the LVK’s inferred merger rate is shown by the magenta solid line, with its 95% confidence interval indicated by the shaded band. When fit with a power-law of the form $(1+z)^{\kappa}$, LVK finds $\kappa = 2.9^{+1.7}_{-1.8}$, while our model is best fit by $\kappa = 1.5$, which falls within their 1σ range. Both values differ from the pure SFR scaling $(1+z)^{2.7}$, reflecting the influence of the delay-time distribution on the redshift evolution of the merger rate density.

We compare LVK’s model with our merger rate evolved over redshift in Figure 10. Our model consistently remains within the 95% confidence interval for inferred rate across various redshifts, which indicates that the merger rate scales with time as the assumed star formation history.

Given that our model incorporates the star formation rate (SFR) history of the universe as a function of redshift, we naturally expect the merger rate of compact objects to vary over cosmic time. The LVK collaboration describes their merger rate using a power-law, $\mathcal{R}(z) \propto (1+z)^{\kappa}$, and notes that their inferred rate tracks the SFR history of the universe (The LIGO Scientific Collaboration et al. 2022). When fit with a power-law, our model yields $\kappa = 1.50$, consistent with the inferred value of $\kappa = 2.9^{+1.7}_{-1.8}$ from LVK. The SFR itself scales as $\propto (1+z)^{2.7}$, indicating that the temporal evolution of the BBH cosmic merger rate is modified by the convolution with the DTD. The specific parameterization for the SFR also introduces some uncertainties (Boesky et al. 2024b,a), particularly when convolved with the DTD, which need to be explored.

3.3. Mass Ratio

We conclude our comparison with the LVK’s binary black hole observations by analyzing how the merger rate depends on the mass ratio of the black holes, $q_{\text{BH}} = \frac{M_2}{M_1}$. To achieve this, we use Equation 3 integrating over the full range of primary masses, M_1 , rather than mass ratio q :

$$\frac{dN_{\text{BBH}}}{dq}(M_{\star}) = C_{\text{N}} \int_{M_{1,l}}^{M_{1,u}} \int_{Z_l}^{Z_u} \rho(Z | M_{\star}) \int_{8M_{\odot}}^{M_u} M_p^{\alpha} p(M_1, q | M_p, Z) dZ dM_p dM_1, \quad (10)$$

where, $p(M_1, q_{\text{BH}} | M_p, Z)$ represents the joint probability of forming a black hole with primary mass M_1 and mass ratio q_{BH} , modeled using a two-dimensional Gaussian kernel density estimation, as described in Section 2.1, conditioned on progenitor mass M_p and metallicity Z . Building on Equation 10, we integrate over the delay-time distribution (DTD) and star formation rate (SFR) to obtain:

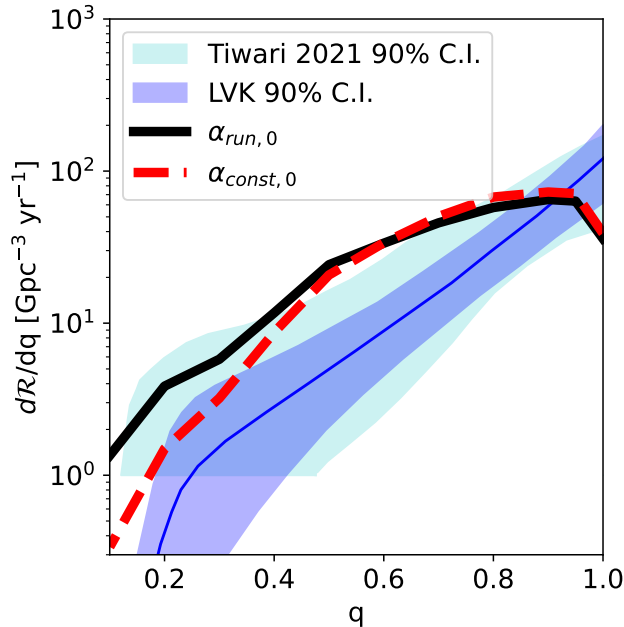


Figure 11. Comparison of the mass ratio distribution $d\mathcal{R}/dq$ from our two population models to the LVK-inferred distribution (dark blue band) and the results from [Tiwari \(2022\)](#) (cyan, showing their 90% C.I.). The red dashed line represents the constant-slope model ($\alpha_{\text{const}} = -2.3$), while the black line shows the running-slope model ($\alpha_{\text{run}} = -2.3 + \log_{10}(M/8M_{\odot})\beta$), with $\beta = 0.7$. As with the primary mass spectrum, the running-slope model aligns more closely with LVK observations. Although our models generally agree with LVK data across most of the mass ratio range, we find a slight overdensity at intermediate q and a slower decline at the lower end of the spectrum. This behavior results from the persistence of high-mass black holes ($\gtrsim 50 M_{\odot}$) in our simulations, which evolve in isolation due to specific orbital dynamics and the secondary’s lower mass, resulting in a slower decline at the lower end of the spectrum compared to LVK observations. The LVK currently employs a simple power-law fit to the mass ratio distribution; however, our results suggest that the true underlying distribution is more complex and may become clearer with future gravitational wave detections.

$$\frac{d\mathcal{R}}{dq} = C_{\text{N}} \int_0^{t_0} \frac{\psi(t_0 - \tau')}{\int_0^{t_0} \psi(t_0 - \tau') dt} P(\tau') \int_{M_{\text{min}}}^{\infty} \frac{dN_{\text{BBH}}(M_{\star}) \phi(M_{\star}) dM_{\star} d\tau'}{dq} \quad (11)$$

Overall, we find broad agreement in the trends between our model and the LVK mass ratio spectrum at $z = 0.0$, as shown in Figure 11. However, it is important to note that the LVK fit assumes a power-law parameterization of the mass ratio of the form $p(q) \propto q^{\beta}$, which may oversimplify the true underlying dependence of the merger rate on the mass ratio. Our model, monotonically increases but tends to overshoot the LVK spectrum. The majority of our systems peak at $q \sim 0.9$ and fall off as q approaches ~ 1 . This deviation is attributed to the increasing power-law behavior used in the LVK parameterization. As more observations are made, we predict that the true distribution of mass ratios will reveal greater complexity, potentially aligning more closely with the predictions of our model.

These results are sensitive to the assumed underlying distribution of the initial mass ratio, q_{ZAMS} , which is sampled following the distribution described in [Sana et al. \(2012\)](#). After applying our selection criteria, the resulting distribution of q_{ZAMS} in our simulations aligns well with empirical observations of massive star populations, as reported in [Moe & Di Stefano \(2017\)](#). Specifically, [Moe & Di Stefano \(2017\)](#) find a strong preference for twins (i.e. $q \sim 1$) and a peak at $q \sim 0.3$. In contrast, our distribution peaks at $q \sim 0.6$, although the overall structure, characterized by a power-law slope at low q , a peak, and a second power-law rise approaching the twin peak, remains consistent with these observational findings.

Furthermore, we show in Figure 13 that the black holes from our simulations, post-cut, prefer mass ratios close to unity. There is also an indication of build-up at $\sim 10 M_{\odot}$, $\sim 20 M_{\odot}$, and $\sim 35 M_{\odot}$. These over-densities correspond to the bumps in the LVK spectrum for the PP and FM models. There is a noticeable gap in the distribution starting near $\sim 25 M_{\odot}$, which extends until $\sim 35 M_{\odot}$, where systems reappear due to the pair instability mechanism. Perhaps this

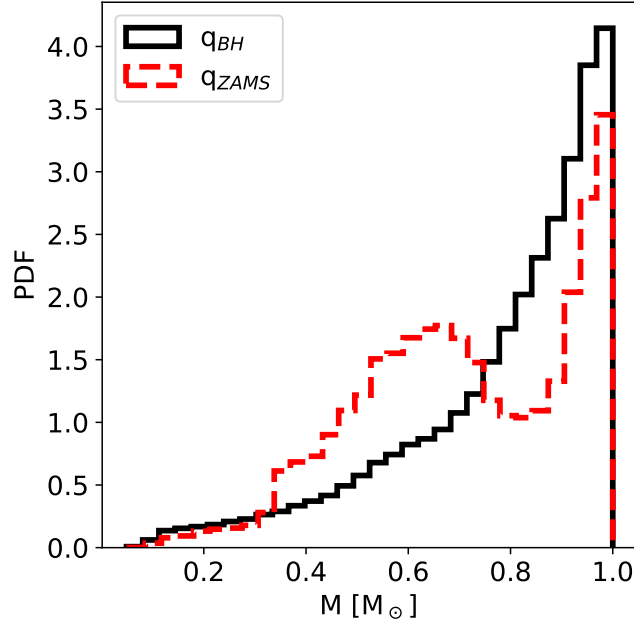


Figure 12. Comparison of the initial stellar mass ratio distribution, q_{ZAMS} , after applying selection cuts, with the mass ratio distribution of the binary black holes from our simulations. The q_{ZAMS} distribution (red dashed line) contains a peak at $q \sim 0.6$, aligning with the observed peak at $q \sim 0.3$ in Moe & Di Stefano (2017) and showing a strong preference for "twins." The q_{BH} distribution follows an increasing power-law trend, indicating a preference for more equal-mass black hole binaries. Note that this is distinct from Figure 11, as no galaxy-dependent quantities are folded into this distribution, only stellar evolution effects.

is suggesting that isolated binaries alone can account for all the structures observed in the black hole mass spectrum. This figure can also be compared with Figure 2 from (Farah et al. 2023) or Figure 7 from (Callister 2024), where they show the inferred two-dimensional underlying mass distribution.

4. CONCLUSION

Our approach, grounded in observed galactic relations, utilizes the SEVN stellar evolution code to construct a model of the binary black hole population and merger rates. We folded in the metallicity distribution that depends on galaxy stellar mass, the galaxy stellar mass function, star formation rate, and delay time distribution to compute the binary black hole merger rate density. Our results show good agreement with the LVK observations overall and will help create better model predictions for comparison to the additional BBH mergers (up to ~ 300) from observing run 4 (Broekgaarden et al. 2024; Kiendrebeogo et al. 2023; Abbott et al. 2020a).

There are significant uncertainties in the various elements of our calculation, including the star formation history, the initial mass function, and the physical processes in stellar evolution theory, such as mixing, wind mass loss, and common envelope phase as modeled by the SEVN code (Iorio et al. 2022). While these factors introduce variability, they also present opportunities to gain insights into the star formation history, initial mass function, and stellar evolution for massive binary stars. Initial strides to systematically quantify the impact of these uncertainties have been made by Broekgaarden et al. (2021), who explored the effects of uncertain stellar evolution physics and star formation histories on binary compact object merger rates and mass distributions. Our aims in this paper are to elucidate how the various elements of the calculation come together to produce the distribution of binary black holes in a simple way, and to highlight the importance of the metallicity distribution in galaxies and other key features summarized below.

The predicted merger rate as a function of redshift is consistent with observations, as shown in Figure 10, where our model lies within the 95% confidence interval across cosmic time. This is encouraging given the simplicity of the model and the reasonable value for the average core collapse supernova rate used to normalize the merger rate. Additionally, the merger rate with respect to the mass ratio shows agreement overall, but has an overabundance of mass ratios of about 0.5. This discrepancy could be due to the power-law approximation assumed in the inference by LVK, as discussed in Section 3.3. In this regard, we note that our initial progenitor distribution from Sana et al. (2012) agrees

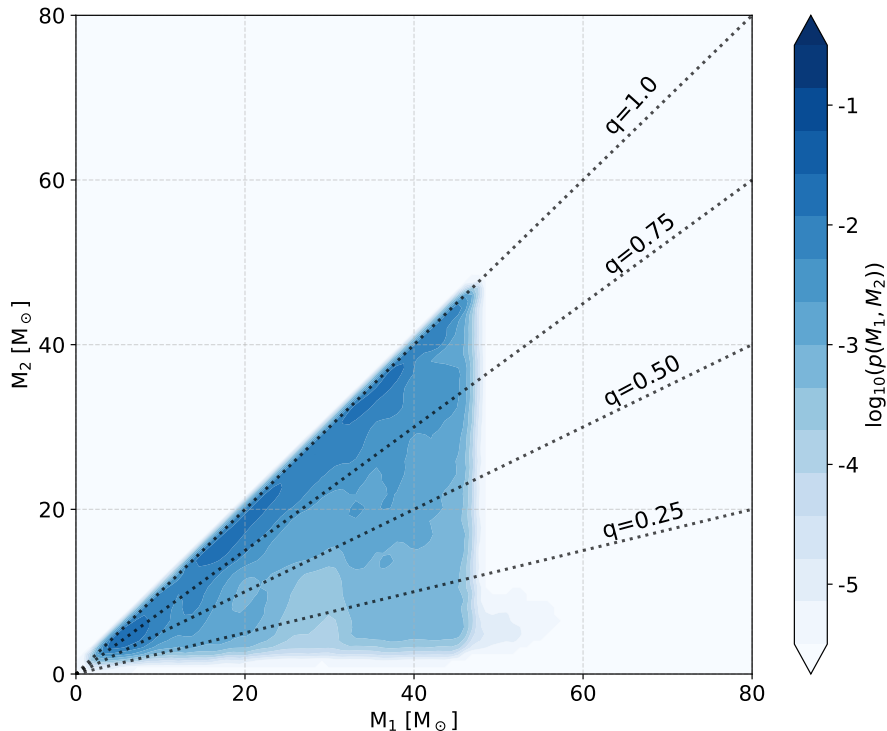


Figure 13. Binary systems tend to cluster toward mass ratios approaching unity. Overdense regions are located at $\sim 10 M_{\odot}$, $\sim 20 M_{\odot}$, and $\sim 35 M_{\odot}$, consistent with the PP and FM parametric models from LVK. The black dotted lines indicate contours of constant q . Note the absence of systems starting at $\sim 25 M_{\odot}$, which lasts until $\sim 35 M_{\odot}$, where systems begin to repopulate due to the pair instability mechanism.

with the massive star mass ratio distribution inferred by [Moe & Di Stefano \(2017\)](#), with only small discrepancies near the first peak.

The black hole mass spectrum, $d\mathcal{R}/dM_1$, has several features rich with information. The smooth tapering at low masses is apparent, driven by binary effects and the decreasing probability of lower-mass black holes being the primary in a BBH system. We obtain a peak at $\sim 20 M_{\odot}$, consistent with the LVK’s FM and PS models. However, the observed abundance of black holes in the $30 - 40 M_{\odot}$ range presents a challenge for the model with a power-law stellar initial mass function.

We explored the possibility that the average IMF is top-heavy by allowing the power-law index of the IMF to vary with mass. We found that a running-slope model ($\alpha = -2.3 + 0.7 \log_{10}(M/8M_{\odot})$) is a better fit to the inferred primary mass distribution. Most of high mass binary black holes in our model arise in dwarf galaxies, which are metal-poor, and hence this result is essentially arguing for a more top-heavy IMF in dwarf galaxies. This finding is qualitatively aligned with observations of the top-heavy IMFs inferred in metal-poor galaxies and globular clusters ([Marks et al. 2012](#); [Geha et al. 2013](#); [Gennaro et al. 2018](#); [Weatherford et al. 2021](#)). Alternatively, these black holes may predominantly form through dynamical capture mechanisms. The impacts of these disparate scenarios on the mass ratio distribution and the redshift distribution may offer clues to distinguish them.

Addressing the high-mass end of the merger-rate spectrum remains a challenge and is an active area of research. Studies such as [Antonini et al. \(2022\)](#); [Torniamenti et al. \(2024\)](#) suggest that the peak at $\sim 35 M_{\odot}$ could be populated by a subpopulation of black holes forming in globular clusters. In our analysis, this bump arises due to the pair instability mechanism and hence becomes more prominent when considering a top-heavy IMF (running-slope model). However, we have treated a galaxy as a monolithic entity, neglecting diverse components such as globular clusters, star clusters, bulges, and disks. These components exhibit varying densities, metallicities and stellar populations, leading to

differences in merger rates and dynamical interactions. This diversity could contribute to filling the mass gap through hierarchical mergers and to the formation of a more prominent peak at $\sim 35 M_{\odot}$. A more granular examination of these factors, set within the framework of galactic relations, is left for future work.

Beyond $50 M_{\odot}$, our model predicts a sharp decline in the number of BBH systems, revealing the well-known mass gap caused by the pair instability mechanism and mass loss in binary systems. Incorporating mergers in dynamically-formed BBHs originating from the single black hole population could help fill this gap. We estimate that an efficiency for these dynamical processes of $\sim 0.01\%$ could impact the high-mass end, making it more comparable to observations up to about $60 M_{\odot}$ in primary black hole mass.

We also direct the reader to previous studies on possible explanations for the high-mass end of the distribution, including population III stars (Farrell et al. 2021; Kinugawa et al. 2021; Liu & Bromm 2020; Safarzadeh & Ramirez-Ruiz 2021), hierarchical mergers (Sedda et al. 2023; Gerosa & Fishbach 2021; Mapelli et al. 2021; Farr et al. 2017; Antonini et al. 2022; Tornamenti et al. 2024), primordial black holes (De Luca et al. 2021), and beyond the Standard Model (BSM) physics (Croon et al. 2020; Sakstein et al. 2020; Ziegler & Freese 2021, 2024; Croon & Sakstein 2024).

In summary, our study demonstrates that a population model grounded in galactic relations, such as the galaxy stellar mass function, metallicity distribution, and star formation rate, can reproduce many of the features of the mass distribution and redshift evolution of BBHs observed by the LVK collaboration. Our modeling suggests that a top-heavy IMF in low-mass metal-poor galaxies would provide a better match to the primary mass spectrum up to about $50 M_{\odot}$. Alternately, we would need to include dynamical capture mechanisms such as those that could happen in globular clusters. Although the uncertainties in stellar evolution and star formation history are still large, our findings demonstrate that most of the black hole mergers observed by LVK can be explained by a simple model that averages over the observed properties of galaxies. This allows for a more robust assessment of the mismatch between the predictions and observations of black holes at the high-mass end.

5. ACKNOWLEDGEMENTS

TBS acknowledges support from the National Science Foundation Graduate Research Fellowship Program under Grant No. 1839285. MK acknowledges support from the National Science Foundation under Grant No. 2210283.

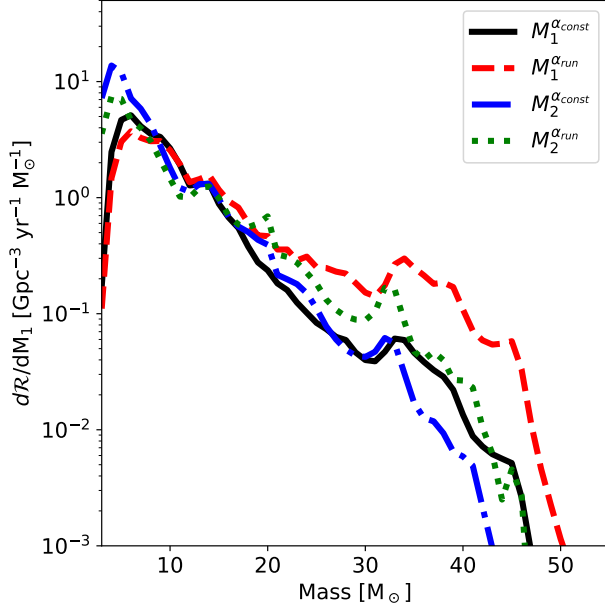
APPENDIX

A. SECONDARY MASSES

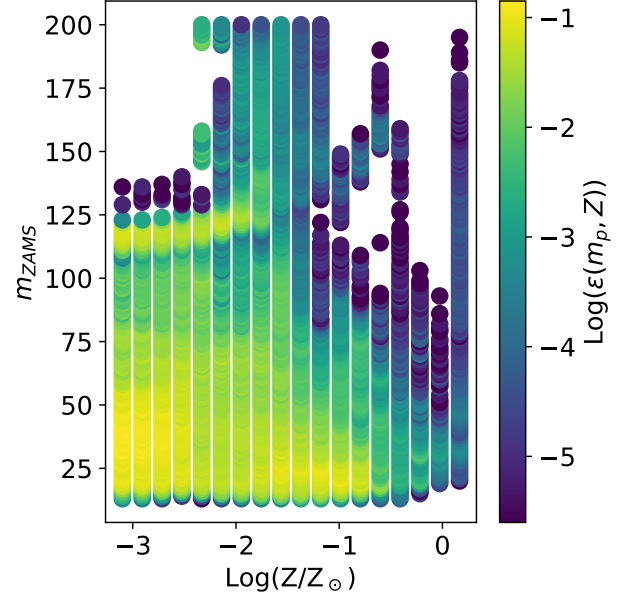
While the primary focus of this paper has been the distribution of primary black hole masses, our model also allows for a detailed examination of the secondary mass distribution. In our simulations, we uniformly sample primary masses M_1 within the range $[10, 200] M_{\odot}$ and assign secondary masses following the mass ratio distribution inferred by Sana et al. (2012), parameterized as $q^{-0.1}$. Using the same methodology outlined in Sections 3.1 and 2.3, we derive the differential merger rate density with respect to the secondary mass, $d\mathcal{R}/dM_2$.

Figure 14 compares the secondary mass spectrum to the primary for both the constant-slope and running-slope IMF models. The secondary mass distribution shows a less pronounced drop-off at lower masses compared to the primary, although it occurs within a similar mass range. The characteristic bump seen in the primary mass spectrum around $\sim 35 M_{\odot}$ is far less prominent in the secondary mass spectrum, highlighting subtle differences in their formation and evolutionary pathways.

For completeness, the right panel of Figure 14 includes the efficiency to create secondary-mass black holes as a function of progenitor mass and metallicity. This function is qualitatively similar to that of the primaries but shows reduced black hole formation from higher-mass stars at higher metallicities. If both stars are very massive (i.e., $\gtrsim 100 M_{\odot}$), they must have a suitable semi-major axis to avoid destabilizing the binary due to their large sizes and high metallicity line-driven winds. As shown, such systems are unlikely to form binary black holes that would merge within a Hubble time, as most secondaries for very massive primaries tend to have lower masses. Although there is some variation across metallicities, this trend remains consistent.



(a) Differential merger rate density for primary and secondary masses.



(b) Efficiency for creating secondary black holes.

Figure 14. (a) Differential merger rate density comparison for primary and secondary masses for both the constant-slope ($\alpha = -2.3$) and running-slope ($\alpha = -2.3 + 0.7 \log_{10}(M/8M_{\odot})$) models. The M_1 distributions are taken from Figure 9. The secondary mass spectrum exhibits a steeper decline and lacks the prominent bump around $\sim 35 M_{\odot}$. Although the primary and secondary masses are drawn from the same population, they display slight spectral differences. (b) The efficiency to create secondary-mass black holes as a function of progenitor mass and metallicity. Note the absence of high-mass progenitors forming secondary black holes at higher metallicity.

REFERENCES

- Abac, A. G., et al. 2024. <https://arxiv.org/abs/2404.04248>
- Abbott, B. P., Abbott, R., Abbott, T. D., et al. 2016, *Physical Review Letters*, 116, 1, doi: [10.1103/PhysRevLett.116.061102](https://doi.org/10.1103/PhysRevLett.116.061102)
- Abbott, B. P., et al. 2019, *Astrophys. J. Lett.*, 882, L24, doi: [10.3847/2041-8213/ab3800](https://doi.org/10.3847/2041-8213/ab3800)
- . 2020a, *Living Rev. Rel.*, 23, 3, doi: [10.1007/s41114-020-00026-9](https://doi.org/10.1007/s41114-020-00026-9)
- Abbott, R., et al. 2020b, *Astrophys. J. Lett.*, 896, L44, doi: [10.3847/2041-8213/ab960f](https://doi.org/10.3847/2041-8213/ab960f)
- Abbott, R., Abbott, T. D., Abraham, S., et al. 2020c, *Phys. Rev. Lett.*, 125, 101102, doi: [10.1103/PhysRevLett.125.101102](https://doi.org/10.1103/PhysRevLett.125.101102)
- . 2020d, *The Astrophysical Journal*, 900, L13, doi: [10.3847/2041-8213/aba493](https://doi.org/10.3847/2041-8213/aba493)
- . 2021a, *Physical Review X*, 11, 021053, doi: [10.1103/PhysRevX.11.021053](https://doi.org/10.1103/PhysRevX.11.021053)
- Abbott, R., et al. 2021b, *Astrophys. J. Lett.*, 915, L5, doi: [10.3847/2041-8213/ac082e](https://doi.org/10.3847/2041-8213/ac082e)
- Antonini, F., Gieles, M., Dosopoulou, F., & Chattopadhyay, D. 2022. <https://arxiv.org/abs/2208.01081>
- Baldry, I. K., Driver, S. P., Loveday, J., et al. 2012, *Monthly Notices of the Royal Astronomical Society*, 421, 621, doi: [10.1111/j.1365-2966.2012.20340.x](https://doi.org/10.1111/j.1365-2966.2012.20340.x)
- Barkat, Z., Rakavy, G., & Sack, N. 1967, *Physical Review Letters*, 18, 379, doi: [10.1103/PhysRevLett.18.379](https://doi.org/10.1103/PhysRevLett.18.379)
- Bavera, S. S., Fragos, T., Qin, Y., et al. 2020, *Astron. Astrophys.*, 635, A97, doi: [10.1051/0004-6361/201936204](https://doi.org/10.1051/0004-6361/201936204)
- Belczynski, K., Heger, A., Gladysz, W., et al. 2016, *Astronomy and Astrophysics*, 594, 1, doi: [10.1051/0004-6361/201628980](https://doi.org/10.1051/0004-6361/201628980)
- Bestenlehner, J. M., Gräfenner, G., Vink, J. S., et al. 2014, *Astronomy & Astrophysics*, 570, A38
- Bestenlehner, J. M., Crowther, P. A., Caballero-Nieves, S. M., et al. 2020, *Monthly Notices of the Royal Astronomical Society*, 499, 1918
- Boesky, A., Broekgaarden, F. S., & Berger, E. 2024a. <https://arxiv.org/abs/2405.01630>
- . 2024b. <https://arxiv.org/abs/2405.01623>
- Bombaci, I. 1996, *A&A*, 305, 871

- Bressan, A., Marigo, P., Girardi, L., et al. 2012, *Monthly Notices of the Royal Astronomical Society*, 427, 127, doi: [10.1111/j.1365-2966.2012.21948.x](https://doi.org/10.1111/j.1365-2966.2012.21948.x)
- Broekgaarden, F. S., Banagiri, S., & Payne, E. 2024, *Astrophys. J.*, 969, 108, doi: [10.3847/1538-4357/ad4709](https://doi.org/10.3847/1538-4357/ad4709)
- Broekgaarden, F. S., et al. 2021, doi: [10.1093/mnras/stac1677](https://doi.org/10.1093/mnras/stac1677)
- Brown, T. M., Tumlinson, J., Geha, M., et al. 2014, *ApJ*, 796, 91, doi: [10.1088/0004-637X/796/2/91](https://doi.org/10.1088/0004-637X/796/2/91)
- Caldwell, N., Walker, M. G., Mateo, M., et al. 2017, *ApJ*, 839, 20, doi: [10.3847/1538-4357/aa688e](https://doi.org/10.3847/1538-4357/aa688e)
- Callister, T. A. 2024. <https://arxiv.org/abs/2410.19145>
- Chen, Y., Bressan, A., Girardi, L., et al. 2015, *Monthly Notices of the Royal Astronomical Society*, 452, 1068, doi: [10.1093/mnras/stv1281](https://doi.org/10.1093/mnras/stv1281)
- Chiti, A., Frebel, A., Ji, A. P., et al. 2018, *ApJ*, 857, 74, doi: [10.3847/1538-4357/aab4fc](https://doi.org/10.3847/1538-4357/aab4fc)
- Collins, M. L. M., Tollerud, E. J., Sand, D. J., et al. 2017, *MNRAS*, 467, 573, doi: [10.1093/mnras/stx067](https://doi.org/10.1093/mnras/stx067)
- Croon, D., McDermott, S. D., & Sakstein, J. 2020, *Phys. Rev. D*, 102, 115024, doi: [10.1103/PhysRevD.102.115024](https://doi.org/10.1103/PhysRevD.102.115024)
- Croon, D., & Sakstein, J. 2024, *Phys. Rev. D*, 109, 103021, doi: [10.1103/PhysRevD.109.103021](https://doi.org/10.1103/PhysRevD.109.103021)
- Crowther, P. A., Schnurr, O., Hirschi, R., et al. 2010, *Mon. Not. Roy. Astron. Soc.*, 408, 731, doi: [10.1111/j.1365-2966.2010.17167.x](https://doi.org/10.1111/j.1365-2966.2010.17167.x)
- De Luca, V., Desjacques, V., Franciolini, G., Pani, P., & Riotto, A. 2021, *Phys. Rev. Lett.*, 126, 051101, doi: [10.1103/PhysRevLett.126.051101](https://doi.org/10.1103/PhysRevLett.126.051101)
- Elbert, O. D., Bullock, J. S., & Kaplinghat, M. 2018, *Monthly Notices of the Royal Astronomical Society*, 473, 1186, doi: [10.1093/mnras/stx1959](https://doi.org/10.1093/mnras/stx1959)
- Fabrizio, M., Merle, T., Thévenin, F., et al. 2012, *PASP*, 124, 519, doi: [10.1086/666480](https://doi.org/10.1086/666480)
- Farah, A. M., Edelman, B., Zevin, M., et al. 2023. <https://arxiv.org/abs/2301.00834>
- Farr, W. M., Sravan, N., Cantrell, A., et al. 2011, *Astrophys. J.*, 741, 103, doi: [10.1088/0004-637X/741/2/103](https://doi.org/10.1088/0004-637X/741/2/103)
- Farr, W. M., Stevenson, S., Coleman Miller, M., et al. 2017, *Nature*, 548, 426, doi: [10.1038/nature23453](https://doi.org/10.1038/nature23453)
- Farrell, E. J., Groh, J. H., Hirschi, R., et al. 2021, *Mon. Not. Roy. Astron. Soc.*, 502, L40, doi: [10.1093/mnrasl/slaa196](https://doi.org/10.1093/mnrasl/slaa196)
- Fowler, W. A., & Hoyle, F. 1964, *The Astrophysical Journal Supplement Series*, 9, 201, doi: [10.1086/190103](https://doi.org/10.1086/190103)
- Frebel, A., Simon, J. D., & Kirby, E. N. 2014, *ApJ*, 786, 74, doi: [10.1088/0004-637X/786/1/74](https://doi.org/10.1088/0004-637X/786/1/74)
- Fryer, C. L., Woosley, S. E., & Heger, A. 2001, *Population (English Edition)*, 20, 372
- Gallazzi, A., Charlot, S., Brinchmann, J., White, S. D., & Tremonti, C. A. 2005, *Monthly Notices of the Royal Astronomical Society*, 362, 41, doi: [10.1111/j.1365-2966.2005.09321.x](https://doi.org/10.1111/j.1365-2966.2005.09321.x)
- García, F., Bunzel, A. S., Chaty, S., Porter, E., & Chassande-Mottin, E. 2021, *Astron. Astrophys.*, 649, A114, doi: [10.1051/0004-6361/202038357](https://doi.org/10.1051/0004-6361/202038357)
- Geha, M., Brown, T. M., Tumlinson, J., et al. 2013, *ApJ*, 771, 29, doi: [10.1088/0004-637X/771/1/29](https://doi.org/10.1088/0004-637X/771/1/29)
- Gennaro, M., Tchernyshyov, K., Brown, T. M., et al. 2018, *ApJ*, 855, 20, doi: [10.3847/1538-4357/aaa973](https://doi.org/10.3847/1538-4357/aaa973)
- Gerosa, D., & Fishbach, M. 2021, *Nature Astron.*, 5, 749, doi: [10.1038/s41550-021-01398-w](https://doi.org/10.1038/s41550-021-01398-w)
- Heger, A., Fryer, C. L., Woosley, S. E., Langer, N., & Hartmann, D. H. 2003, *Astrophys. J.*, 591, 288, doi: [10.1086/375341](https://doi.org/10.1086/375341)
- Iorio, G., et al. 2022. <https://arxiv.org/abs/2211.11774>
- Jayasinghe, T., et al. 2021, *Mon. Not. Roy. Astron. Soc.*, 504, 2577, doi: [10.1093/mnras/stab907](https://doi.org/10.1093/mnras/stab907)
- Ji, A. P., Frebel, A., Simon, J. D., & Geha, M. 2016, *ApJ*, 817, 41, doi: [10.3847/0004-637X/817/1/41](https://doi.org/10.3847/0004-637X/817/1/41)
- Johnson, B. D., et al. 2013, *Astrophys. J.*, 772, 8, doi: [10.1088/0004-637X/772/1/8](https://doi.org/10.1088/0004-637X/772/1/8)
- Kalogera, V., & Baym, G. 1996, *Astrophys. J. Lett.*, 470, L61, doi: [10.1086/310296](https://doi.org/10.1086/310296)
- Kiendrebeogo, R. W., et al. 2023, *Astrophys. J.*, 958, 158, doi: [10.3847/1538-4357/acfcbl](https://doi.org/10.3847/1538-4357/acfcbl)
- Kim, D., Jerjen, H., Geha, M., et al. 2016, *ApJ*, 833, 16, doi: [10.3847/0004-637X/833/1/16](https://doi.org/10.3847/0004-637X/833/1/16)
- Kinugawa, T., Nakamura, T., & Nakano, H. 2021, *Mon. Not. Roy. Astron. Soc.*, 501, L49, doi: [10.1093/mnrasl/slaa191](https://doi.org/10.1093/mnrasl/slaa191)
- Kirby, E. N., Cohen, J. G., Guhathakurta, P., et al. 2013, *Astrophysical Journal*, 779, doi: [10.1088/0004-637X/779/2/102](https://doi.org/10.1088/0004-637X/779/2/102)
- Kirby, E. N., Cohen, J. G., Simon, J. D., et al. 2017, *ApJ*, 838, 83, doi: [10.3847/1538-4357/aa6570](https://doi.org/10.3847/1538-4357/aa6570)
- Kirby, E. N., Simon, J. D., & Cohen, J. G. 2015, *ApJ*, 810, 56, doi: [10.1088/0004-637X/810/1/56](https://doi.org/10.1088/0004-637X/810/1/56)
- Koposov, S. E., Casey, A. R., Belokurov, V., et al. 2015, *ApJ*, 811, 62, doi: [10.1088/0004-637X/811/1/62](https://doi.org/10.1088/0004-637X/811/1/62)
- Koposov, S. E., Walker, M. G., Belokurov, V., et al. 2018, *MNRAS*, 479, 5343, doi: [10.1093/mnras/sty1772](https://doi.org/10.1093/mnras/sty1772)
- Kroupa, P. 2001, *Monthly Notices of the Royal Astronomical Society*, 322, 231, doi: [10.1046/j.1365-8711.2001.04022.x](https://doi.org/10.1046/j.1365-8711.2001.04022.x)
- Kumamoto, J., Fujii, M. S., & Tanikawa, A. 2020, *MNRAS*, 495, 4268, doi: [10.1093/mnras/staa1440](https://doi.org/10.1093/mnras/staa1440)
- Li, T. S., Simon, J. D., Drlica-Wagner, A., et al. 2017, *ApJ*, 838, 8, doi: [10.3847/1538-4357/aa6113](https://doi.org/10.3847/1538-4357/aa6113)

- Li, T. S., Simon, J. D., Pace, A. B., et al. 2018, *ApJ*, 857, 145, doi: [10.3847/1538-4357/aab666](https://doi.org/10.3847/1538-4357/aab666)
- Li, W., Chornock, R., Leaman, J., et al. 2011, *MNRAS*, 412, 1473, doi: [10.1111/j.1365-2966.2011.18162.x](https://doi.org/10.1111/j.1365-2966.2011.18162.x)
- Liu, B., & Bromm, V. 2020, *Astrophys. J. Lett.*, 903, L40, doi: [10.3847/2041-8213/abc552](https://doi.org/10.3847/2041-8213/abc552)
- Longeard, N., Martin, N., Starkenburg, E., et al. 2018, *MNRAS*, 480, 2609, doi: [10.1093/mnras/sty1986](https://doi.org/10.1093/mnras/sty1986)
- Madau, P., & Fragos, T. 2017, *The Astrophysical Journal*, 840, 39, doi: [10.3847/1538-4357/aa6af9](https://doi.org/10.3847/1538-4357/aa6af9)
- Mapelli, M., Santoliquido, F., Bouffanais, Y., et al. 2021, *Symmetry*, 13, 1678, doi: [10.3390/sym13091678](https://doi.org/10.3390/sym13091678)
- Mapelli, M., Spera, M., Montanari, E., et al. 2020, *The Astrophysical Journal*, 888, 76, doi: [10.3847/1538-4357/ab584d](https://doi.org/10.3847/1538-4357/ab584d)
- Marigo, P., Girardi, L., Bressan, A., et al. 2017, *The Astrophysical Journal*, 835, 77, doi: [10.3847/1538-4357/835/1/77](https://doi.org/10.3847/1538-4357/835/1/77)
- Marks, M., Kroupa, P., Dabringhausen, J., & Pawlowski, M. S. 2012, *Mon. Not. Roy. Astron. Soc.*, 422, 2246, doi: [10.1111/j.1365-2966.2012.20767.x](https://doi.org/10.1111/j.1365-2966.2012.20767.x)
- Moe, M., & Di Stefano, R. 2017, *ApJS*, 230, 15, doi: [10.3847/1538-4365/aa6fb6](https://doi.org/10.3847/1538-4365/aa6fb6)
- Mucciarelli, A., Bellazzini, M., Ibata, R., et al. 2017, *A&A*, 605, A46, doi: [10.1051/0004-6361/201730707](https://doi.org/10.1051/0004-6361/201730707)
- Nguyen, C. T., Costa, G., Girardi, L., et al. 2022, *A&A*, 665, A126, doi: [10.1051/0004-6361/202244166](https://doi.org/10.1051/0004-6361/202244166)
- Ozel, F., Psaltis, D., Narayan, R., & McClintock, J. E. 2010, *Astrophys. J.*, 725, 1918, doi: [10.1088/0004-637X/725/2/1918](https://doi.org/10.1088/0004-637X/725/2/1918)
- Portegies Zwart, S. F., & McMillan, S. L. W. 2000, *ApJL*, 528, L17, doi: [10.1086/312422](https://doi.org/10.1086/312422)
- Qin, Y., Fragos, T., Meynet, G., et al. 2018, *Astron. Astrophys.*, 616, A28, doi: [10.1051/0004-6361/201832839](https://doi.org/10.1051/0004-6361/201832839)
- Rezzolla, L., Most, E. R., & Weih, L. R. 2018, *Astrophys. J. Lett.*, 852, L25, doi: [10.3847/2041-8213/aaa401](https://doi.org/10.3847/2041-8213/aaa401)
- Safarzadeh, M., & Ramirez-Ruiz, E. 2021. <https://arxiv.org/abs/2105.08746>
- Sakstein, J., Croon, D., McDermott, S. D., Straight, M. C., & Baxter, E. J. 2020, *Phys. Rev. Lett.*, 125, 261105, doi: [10.1103/PhysRevLett.125.261105](https://doi.org/10.1103/PhysRevLett.125.261105)
- Sana, H., Gosset, E., Naze, Y., Rauw, G., & Linder, N. 2008, *Mon. Not. Roy. Astron. Soc.*, 386, 447, doi: [10.1111/j.1365-2966.2008.13037.x](https://doi.org/10.1111/j.1365-2966.2008.13037.x)
- Sana, H., De Mink, S. E., De Koter, A., et al. 2012, *Science*, 337, 444, doi: [10.1126/science.1223344](https://doi.org/10.1126/science.1223344)
- Schiebelbein-Zwack, A., & Fishbach, M. 2024. <https://arxiv.org/abs/2403.17156>
- Sedda, M. A., Naoz, S., & Kocsis, B. 2023, *Universe*, 9, 138, doi: [10.3390/universe9030138](https://doi.org/10.3390/universe9030138)
- Simon, J. D. 2019, *ARA&A*, 57, 375, doi: [10.1146/annurev-astro-091918-104453](https://doi.org/10.1146/annurev-astro-091918-104453)
- Simon, J. D., et al. 2015, *Astrophys. J.*, 808, 95, doi: [10.1088/0004-637X/808/1/95](https://doi.org/10.1088/0004-637X/808/1/95)
- Simon, J. D., Li, T. S., Drlica-Wagner, A., et al. 2017, *ApJ*, 838, 11, doi: [10.3847/1538-4357/aa5be7](https://doi.org/10.3847/1538-4357/aa5be7)
- Spera, M., & Mapelli, M. 2017, *Monthly Notices of the Royal Astronomical Society*, 470, 4739, doi: [10.1093/mnras/stx1576](https://doi.org/10.1093/mnras/stx1576)
- Spera, M., Mapelli, M., & Bressan, A. 2015, *Monthly Notices of the Royal Astronomical Society*, 451, 4086, doi: [10.1093/mnras/stv1161](https://doi.org/10.1093/mnras/stv1161)
- Spera, M., Mapelli, M., Giacobbo, N., et al. 2019, *Monthly Notices of the Royal Astronomical Society*, 485, 889, doi: [10.1093/mnras/stz359](https://doi.org/10.1093/mnras/stz359)
- Stefanon, M., Labbé, I., Oesch, P. A., et al. 2021, *ApJS*, 257, 68, doi: [10.3847/1538-4365/ac2498](https://doi.org/10.3847/1538-4365/ac2498)
- Tang, J., Bressan, A., Rosenfield, P., et al. 2014, *Monthly Notices of the Royal Astronomical Society*, 445, 4287, doi: [10.1093/mnras/stu2029](https://doi.org/10.1093/mnras/stu2029)
- The LIGO Scientific Collaboration, the Virgo Collaboration, & the KAGRA Collaboration. 2022, doi: [10.48550/arXiv.2111.03634](https://doi.org/10.48550/arXiv.2111.03634)
- The LIGO Scientific Collaboration, the Virgo Collaboration, Abbott, B. P., et al. 2019, *Physical Review X*, 9, 031040, doi: [10.1103/PhysRevX.9.031040](https://doi.org/10.1103/PhysRevX.9.031040)
- The LIGO Scientific Collaboration, the Virgo Collaboration, the KAGRA Collaboration, et al. 2021, *arXiv e-prints*, arXiv:2111.03606. <https://arxiv.org/abs/2111.03606>
- Tiwari, V. 2022, *Astrophys. J.*, 928, 155, doi: [10.3847/1538-4357/ac589a](https://doi.org/10.3847/1538-4357/ac589a)
- Torniamenti, S., Mapelli, M., Périgois, C., et al. 2024. <https://arxiv.org/abs/2401.14837>
- Walker, M. G., Mateo, M., Olszewski, E. W., et al. 2016, *ApJ*, 819, 53, doi: [10.3847/0004-637X/819/1/53](https://doi.org/10.3847/0004-637X/819/1/53)
- Weatherford, N. C., Fragione, G., Kremer, K., et al. 2021, *Astrophys. J. Lett.*, 907, L25, doi: [10.3847/2041-8213/abd79c](https://doi.org/10.3847/2041-8213/abd79c)
- Weaver, J. R., Davidzon, I., Toft, S., et al. 2023, *A&A*, 677, A184, doi: [10.1051/0004-6361/202245581](https://doi.org/10.1051/0004-6361/202245581)
- Willman, B., Geha, M., Strader, J., et al. 2011, *AJ*, 142, 128, doi: [10.1088/0004-6256/142/4/128](https://doi.org/10.1088/0004-6256/142/4/128)
- Woosley, S. E. 2017, *The Astrophysical Journal*, 836, 244, doi: [10.3847/1538-4357/836/2/244](https://doi.org/10.3847/1538-4357/836/2/244)
- . 2019, *The Astrophysical Journal*, 878, 49, doi: [10.3847/1538-4357/ab1b41](https://doi.org/10.3847/1538-4357/ab1b41)
- Woosley, S. E., Blinnikov, S., & Heger, A. 2007, *Nature*, 450, 390, doi: [10.1038/nature06333](https://doi.org/10.1038/nature06333)

- Woosley, S. E., & Heger, A. 2015, Very Massive Stars in the Local Universe, 199
- . 2021, *Astrophys. J. Lett.*, 912, L31,
doi: [10.3847/2041-8213/abf2c4](https://doi.org/10.3847/2041-8213/abf2c4)
- Ziegler, J., & Freese, K. 2021, *Phys. Rev. D*, 104, 043015,
doi: [10.1103/PhysRevD.104.043015](https://doi.org/10.1103/PhysRevD.104.043015)
- . 2024, *Phys. Rev. D*, 109, 103042,
doi: [10.1103/PhysRevD.109.103042](https://doi.org/10.1103/PhysRevD.109.103042)